A new floating node-based element formulation for modelling pressure-driven fracture

Kocaman, E. S.; Chen, B. Y.; Pinho, S. T.

DOI
10.1016/j.cma.2024.117482

Publication date
2025

Document Version
Final published version

Published in
Computer Methods in Applied Mechanics and Engineering

Citation (APA)
Kocaman, E. S., Chen, B. Y., & Pinho, S. T. (2025). A new floating node-based element formulation for modelling pressure-driven fracture. *Computer Methods in Applied Mechanics and Engineering*, *433*, Article 117482. https://doi.org/10.1016/j.cma.2024.117482

Computer Methods in Applied Mechanics and Engineering 433 (2025) 117482

Contents lists available at ScienceDirect

Comput. Methods Appl. Mech. Engrg.

journal homepage: www.elsevier.com/locate/cma

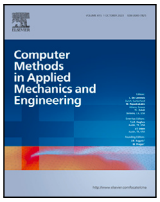

A new floating node-based element formulation for modelling pressure-driven fracture

E.S. Kocaman [a,*], B.Y. Chen [b], S.T. Pinho [c]

[a] *Department of Civil Engineering, Bogazici University, Bebek, Besiktas, Istanbul 34342, Turkiye*
[b] *Faculty of Aerospace Engineering, Delft University of Technology, Kluyverweg 1, 2629 HS Delft, The Netherlands*
[c] *Department of Aeronautics, South Kensington Campus, Imperial College London, London SW7 2AZ, United Kingdom*

ARTICLE INFO

Keywords:
Finite element method
Pressure-driven fracture
Pressure vessels
Floating node method
Multi-physics adaptive modelling

ABSTRACT

When simulating pressure-driven fracture with the Finite Element Method (FEM), significant difficulties can arise upon representing newly formed complex damage surfaces and their concurrent crack face loading. Application of this loading can also be required when additional physics is involved as in the case of hydraulic fracture where fluid physics inside a damage need to be considered. This paper presents a new Finite Element based practical numerical framework which can model pressure-driven fractures as they form on-the-fly without remeshing. The exact location of physical discontinuities passing through the element domain can be represented in the numerical model. The numerical framework can be implemented as a user-defined element and can be integrated into any FE package. A new element (called *pressure* element) is formulated with the capability to apply pressure and associated forces onto the crack surfaces in an adaptive manner. This element is verified using relevant examples from literature. The framework can also be configured for multi-physics problems where crack face loading is dictated by an additional physics. The element formulation is then extended for multi-physics problems involving fluid–solid interaction. The formulation provides the capability for multi-physics coupling adaptively as the crack propagates. The element is used to successfully simulate a test case from literature using different solution procedures (iterative and simultaneous). This element is also used to model failure in different pressure vessel problems to demonstrate its potential use in structural applications. A new higher-scale *vessel* element is developed which can represent different size, partitioning and failure states of composite vessel systems at element level. Composite vessel failure involving high number of pressurized cracks and delaminations as well as their interaction is modelled, and burst pressures are predicted for different vessel systems. The proposed numerical framework can be used towards designing more damage-tolerant vessels critical for the sustainable propulsion technologies.

1. Introduction

1.1. *Background and motivation*

Hydraulic fracture is the process where a crack is propagated by a pressurized fluid acting on the crack surface. There are various structures that are exposed to pressurized fluids such as fuel tanks and submarines which can lead to damage [1,2]. Damage

---

[*] Corresponding author.
E-mail address: esatselim.kocaman@bogazici.edu.tr (E.S. Kocaman).

https://doi.org/10.1016/j.cma.2024.117482
Received 30 July 2024; Received in revised form 16 October 2024; Accepted 16 October 2024

analysis of these structures is important to account for the effect of the fluid behaviour on the design. Moreover, hydraulic fracture has gained strong interest in recent years from the oil and gas industry [3,4]. One of the most prominent applications of pressure-driven fracture problems involve pressure vessels. In accordance with the net zero emission targets set by various new sustainability incentives, fuel systems involving compressed gas storage are gaining increased prominence in various industries such as automotive, transportation and aeronautics [1,2]. Particularly in aeronautics, hydrogen storage has become a promising technology for more sustainable, non-fossil based propulsion. Pressure vessels are essential for the realization of these technologies. Understanding and modelling pressure-driven failure of these structures are particularly crucial to design lighter and more damage-tolerant vessels.

There is a strong interest in literature to model pressure-driven failure using both analytical and numerical approaches [1–13]. Particular interest lies in FE-based models for their capability to simulate complex pressure-driven fracture processes where analytical solutions can be difficult to attain. Significant amount of research is dedicated for pressure vessel failure modelling which typically involves smeared damage approaches [3,5,6] and micromechanics failure models [7–9]. FE-based explicit crack modelling approaches has also been explored for vessel failure applications [10–12].

The pressure-driven problems are also explored for multi-physics problems. Modelling hydraulic fracture is among the most prominent of such problems and many approaches have been proposed in the literature that use different damage modelling techniques such as FEM [3,14–24], Phase Field Method [25–28], Peridynamics [29–31], Boundary Element Method [32,33], and Displacement Discontinuity Method [34–37]. These studies consider various aspects of multi-physics problems such as non-Newtonian lubrication theory, non-planar fracture growth, and generalized asymptotes for different propagation regimes, each having their own advantages and disadvantages. Considering the academic and industrial significance of the Finite Element based approaches and particularly the advanced techniques that does not require remeshing (XFEM and PNM), they constitute the focus of this study. Various techniques are proposed based on XFEM [3,14–18] and PNM [19,20] which provide important capabilities and can be implemented using the available commercial FE packages. Furthermore, for more effective FE-based crack modelling, zero-thickness elements are developed to capture the fluid physics inside the crack and deal with the associated fluid–solid coupling [22,23,38,39]; here, one of the main purposes is to gain more accuracy by accounting the direct interaction between the physical crack discontinuities and the fluid. There is a comprehensive multi-physics literature involving many papers that utilize XFEM and PNM considering wide range of aspects. The use of XFEM and PNM enables hydraulic fracture modelling that does not require re-meshing. However, these methods are unable to represent the exact location of physical discontinuities that can pass through the element domain [40,41] and as a result, their integration with zero thickness elements for fluid–solid coupling is not straightforward. As the crack and fluid propagates in an elastic medium, whose path is not known a priori, difficulties can arise to deal with the evolving topology and multi-physics as well as associated new Degrees of Freedom (DoF) in an effective manner. Considering the vast literature involving XFEM and PNM, exploring new FE-based approaches [40] is critical as they can provide new practical numerical frameworks with significant advantages for pressure-driven fracture.

Exploring new methodologies and numerical frameworks is vital to develop versatile and robust methodologies for pressure-driven fracture modelling of structures. Towards this end, ideally, a numerical framework should not need re-meshing as its implementation can be rather complex. It should have the capability to represent exact physical location of any discontinuity due to damage whose position is not known a priori before a numerical analysis. Accounting exact physical discontinuity positions is critical in non-remeshing techniques (XFEM, PNM) for better accuracy as demonstrated in the literature [40]. Moreover, the framework needs to be able to introduce zero thickness elements that can apply pressure to newly formed complex damage surfaces. It should also deal with the fluid physics and implement the solid–fluid coupling in an adaptive and practical manner as the pressure drives the damage propagation. To achieve all these, the framework needs to be able introduce new DoFs on-the-fly for either the emerged new physics or discontinuities during a simulation. In this work, a new finite element (*pressure* element) is proposed capable of all these features. We explore a recent node technology named Floating Nodes [40] as a starting point to formulate models that has the aforementioned capabilities to simulate pressure-driven fracture more effectively. In addition, the formulation is extended for structural problems whereby a new higher-scale *vessel* element is developed. This element can provide a practical platform to model pressure vessel failure considering different size, partitioning and failure scenarios. It can be applied in the simulation of pressure vessel systems considering a large number of damage and their concurrent crack face loading at element level.

1.2. Outline

In this paper, before formulating the proposed *pressure* element and the associated numerical framework, we establish the background by introducing the FNM and its integration with fundamental damage modelling approaches i.e. Virtual Crack Closure Technique (VCCT) and Cohesive Zones, formulations for cracked solid body and standard cohesive element in Section 2. This section is followed by the formulation of the *pressure* element (Section 3) which enables adaptive crack face loading as the crack emerge on-the-fly during a numerical analysis. The developed *pressure* element inherently contains cohesive zones which can be deactivated based on the analysed problem. This stage constitutes a first step towards the *pressure* element's extended formulation for multi-physics problems.

After this step, we extend *pressure* element formulation for multi-physics problems in Section 4. Considering its prominence among various multi-physics problems, hydraulic fracture modelling is selected for verification of the multi-physics *pressure* element. Such coupled multi-physics problems involving fluid–solid interaction can be solved by either iterative or simultaneous procedures. The developed numerical framework can apply both of these procedures. In the iterative procedure, the solid and fluid parts of the problem are solved separately (by constructing two different FE systems) and coupled via a Picard iteration scheme using the solutions from the individual parts. In the simultaneous procedure, DoF are used for both pressure and displacement, and the

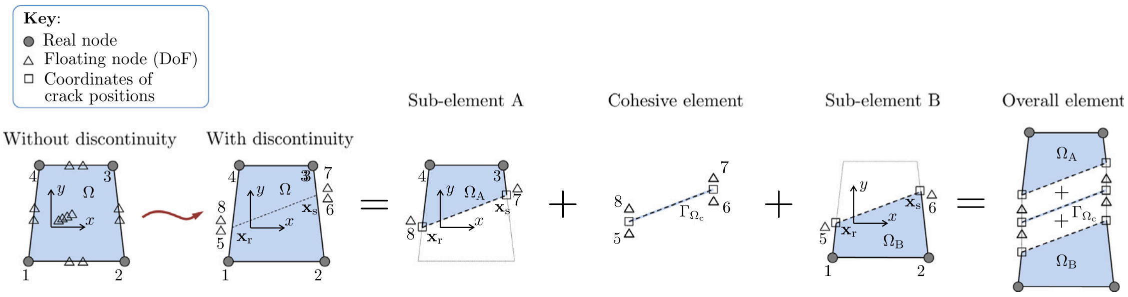

Fig. 1. Overview of the Floating node method, after [40].

problem is solved for all DoFs at the same time. Considering its suitability to develop multi-physics formulation for the *pressure* element, simultaneous procedure is implemented in Section 4. Details of the implementation of the numerical solution procedures are provided in Section 5.

These formulations are verified using several different problems that use different damage propagation approaches (VCCT or cohesive zones) in Sections 6–9. In Section 6, we verify the adaptive crack face loading capability of *pressure* elements using VCCT. After this step, we verify the multi-physics *pressure* elements using both of the solution procedures in Section 7. To demonstrate the capability of *pressure* elements in a industrially relevant critical structural problem, we apply them in the failure modelling of pressure vessels. In Section 8, we use *pressure* element to capture single crack propagation in a pressure vessel using VCCT. Then in Section 9, we apply these elements to a more comprehensive failure analysis of pressure vessels involving high number of cohesive cracks and delamination as well as their interaction. For this important class of structural problems, we also propose a novel *vessel* element for practical modelling of vessel failure in Section 9 and provide valuable insights on vessel failure mechanisms. The paper is finalized with the overall conclusions in Section 10.

2. Background formulations

2.1. Floating node method

In Fig. 1, FNM [40–48] technology is illustrated. Basically, in addition to standard nodes of a finite element, new nodes are introduced to the element associated with different geometrical (topological) entities, such as edges, surfaces or volumes. These floating nodes are not tied to an initial position. When a discontinuity passes through the element, additional Degrees of Freedom (DoFs) are typically needed to represent the discontinuity. In FNM, these floating nodes are assigned to the positions of the discontinuities and corresponding sub-elements are formed inside the main element (Fig. 1). Then, for all sub-elements, typical finite element calculations are performed.

By utilizing different configuration of floating nodes, new enrichment schemes can be devised for various applications [40–48]. In the literature, FNM has been successfully integrated with the progressive damage simulation techniques such as cohesive elements and Virtual Crack Closure Technique (VCCT) [40] which is detailed in the following section.

2.2. Implementation of progressive damage simulation techniques with FNM

2.2.1. Introduction

Cohesive zone models and VCCT are both very commonly used to represent crack growth numerically. The application of these with FNM is explained in this section.

2.2.2. Application of cohesive zone models using FNM

Cohesive Zone Models (CZM) [49] introduce a cohesive zone around a crack tip region composed of initially coinciding surfaces that are separated by applied tractions. The models impose a constitutive law which relates the tractions to the respective separation of the initially-coinciding surfaces.

Using FNM, cohesive cracks can be integrated to a cracked element as shown in Fig. 1. Considering an element that has failed and partitioned into two regions (Ω_A and Ω_B), a cohesive sub-element can easily be introduced to the element along the discontinuity Γ_{Ω_c} (see Fig. 1). The overall stiffness matrix for the element then becomes

$$\mathbf{K}_{\text{all}} = \int_{\Omega_A} \mathbf{B}_A^T \mathbf{D} \mathbf{B}_A \, d\Omega + \int_{\Omega_B} \mathbf{B}_B^T \mathbf{D} \mathbf{B}_B \, d\Omega + \int_{\Gamma_{\Omega_c}} \mathbf{N}_{CE}^T \mathbf{D}_{CE} \mathbf{N}_{CE} \, d\Gamma_c, \tag{1}$$

where $\mathbf{B}_A$ and $\mathbf{B}_B$ are strain–displacement matrices for the domains Ω_A and Ω_B. $\mathbf{N}_{CE}$ refers to the shape function matrix for the cohesive element that relates the nodal DoFs along Γ_{Ω_c} to the separations and $\mathbf{D}_{CE}$ represents to the constitutive matrix that relates the cohesive traction to the respective displacement jumps.

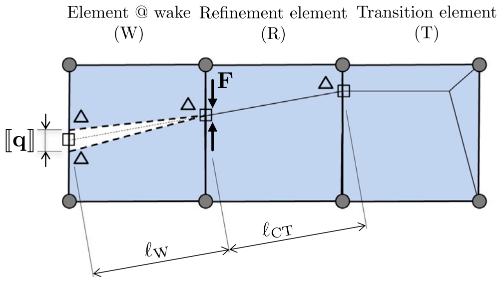

Fig. 2. Implementation of VCCT with FNM, from [40].

Thus, the floating nodes along the surface Γ_{Ω_c} can directly represent the physical discontinuity and interpolate the displacement jumps across the cohesive interface. Finally, the stiffness matrix of the cohesive sub-element (or any other zero thickness element) can be assembled to the stiffness matrix of the overall element, together with those of Ω_A and Ω_B as shown in Eq. (1).

For the cohesive zones in this study, a standard bi-linear law was used with a typical quadratic stress interaction initiation criterion (using the normal strength Y and shear strength S). To determine the critical energy release rate G_c of cohesive zones, we use the B-K criterion

$$G_c = G_{Ic} + (G_{IIc} - G_{Ic})(G_{II}/G_I + G_{II})^{\eta_{BK}}, \tag{2}$$

where G_I and G_{II} are the calculated energy release rates in mode I and mode II from the numerical model, G_{Ic} and G_{IIc} are the critical energy release rates in mode I and II, and η_{BK} is the experimental interaction parameter.

2.2.3. Application of VCCT using FNM

The numerical representation of a crack is shown in Fig. 2. According to VCCT, the energy release rates for mode I and mode II are given respectively by [50]:

$$G_I = \frac{1}{2A_W} F_n \llbracket q_n \rrbracket \left(\frac{A_W}{A_{CT}}\right)^{1/2}, \tag{3}$$

$$G_{II} = \frac{1}{2A_W} F_t \llbracket q_t \rrbracket \left(\frac{A_W}{A_{CT}}\right)^{1/2}, \tag{4}$$

where F_n and F_t are the components of force $\mathbf{F}$ in the normal and tangential directions, and $\llbracket q_n \rrbracket$ and $\llbracket q_t \rrbracket$ are the components of displacement jump $\llbracket \mathbf{q} \rrbracket$ in the normal and tangential directions of the crack, respectively [40]. In addition, A_W represents the crack surface area in the wake element (for a 2-dimensional problem, $A_W = \ell_W b$, where ℓ_W is the length of the discontinuity in the wake element as shown in Fig. 2 and b is the thickness of the domain) and A_{CT} is the crack surface area in the refinement element (for a 2 dimensional problem, $A_{CT} = \ell_{CT} b$, where ℓ_{CT} is the length of the discontinuity in the refinement element as shown in Fig. 2). Using the energy release rates calculated with Eqs. (3) and (4), we can employ a criterion of the form

$$f\left(G_I, G_{II}, G_{Ic}, G_{IIc}, \eta\right) = 0, \tag{5}$$

where G_{Ic}, G_{IIc} and η are relevant material properties, to decide whether the crack should propagate. When crack propagation occurs, the elements along the crack path can be partitioned accordingly using the FNM. To determine the critical energy release rate of crack propagation, we use the B-K criterion whereby Eq. (5) becomes Eq. (2).

2.3. Modelling of a cracked solid body

2.3.1. Weak formulation

A solid body (with a domain Ω) containing a crack (with a domain Γ_c) is shown in Fig. 3(a). Neumann and Dirichlet boundary conditions are applied to the domain boundaries Γ_N and Γ_D, respectively. $\boldsymbol{\tau}_N$ is the applied traction and $\mathbf{u}_D$ is the applied displacement. The crack domain Γ_c contains initially-coinciding upper and lower surfaces, Γ_c^+ and Γ_c^-, respectively. The crack surfaces may be exposed to tractions $\boldsymbol{\tau}_c^+$ and $\boldsymbol{\tau}_c^-$. Considering body forces $\mathbf{b}$ applied to the solid domain, the weak formulation for the static equilibrium of the solid body can be written as

$$\int_{\Gamma_N} \delta\mathbf{u}^T \boldsymbol{\tau}_N \, d\Gamma + \int_{\Gamma_c^+} (\delta\mathbf{u}^+)^T \boldsymbol{\tau}_c^+ \, d\Gamma + \int_{\Gamma_c^-} (\delta\mathbf{u}^-)^T \boldsymbol{\tau}_c^- \, d\Gamma - \int_{\Omega} \nabla \cdot \delta\mathbf{u}^T \boldsymbol{\sigma} \, d\Omega + \int_{\Omega} \delta\mathbf{u}^T \mathbf{b} \, d\Omega = 0, \tag{6}$$

where $\boldsymbol{\sigma}$ is the Cauchy stress tensor, $\delta\mathbf{u}$ is the variation of displacements $\mathbf{u}$ with $\delta\mathbf{u}^+$ and $\delta\mathbf{u}^-$ referring to the variation of displacement specifically on the upper and lower side of the cohesive crack.

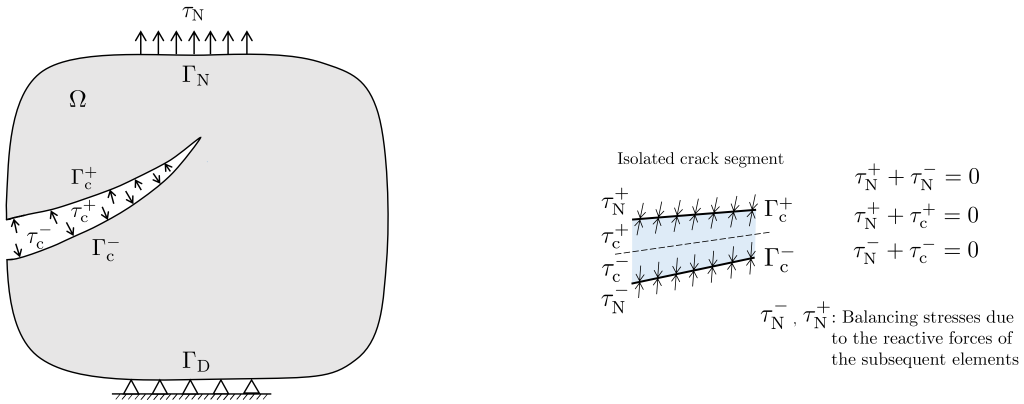

(a) 2D medium with a crack.

(b) A small segment of the crack in equilibrium with the external tractions.

Fig. 3. 2D medium with a crack exposed to crack face loading.

2.3.2. Weak formulation for a pressurized crack segment

Considering now the small segment of the crack with domain Γ_{c} (see Fig. 3(b)) that is connected to the solid domain, both surfaces of the segment will experience tractions. The surfaces of this isolated crack segment are exposed to tractions $\boldsymbol{\tau}_{\mathrm{c}}^{+}$ and $\boldsymbol{\tau}_{\mathrm{c}}^{-}$ which will be balanced by the tractions $\boldsymbol{\tau}_{\mathrm{N}}^{+}$ and $\boldsymbol{\tau}_{\mathrm{N}}^{-}$ due reaction forces of the subsequent elements in the solid body as shown in Fig. 3(b). Then, the virtual work of these tractions acting on both surfaces can be written as

$$\int_{\Gamma_{\mathrm{c}}^{+}} (\delta\mathbf{u}^{+})^{\mathrm{T}} \boldsymbol{\tau}_{\mathrm{N}}^{+} \,\mathrm{d}\Gamma + \int_{\Gamma_{\mathrm{c}}^{-}} (\delta\mathbf{u}^{-})^{\mathrm{T}} \boldsymbol{\tau}_{\mathrm{N}}^{-} \,\mathrm{d}\Gamma + \int_{\Gamma_{\mathrm{c}}^{+}} (\delta\mathbf{u}^{+})^{\mathrm{T}} \boldsymbol{\tau}_{\mathrm{c}}^{+} \,\mathrm{d}\Gamma + \int_{\Gamma_{\mathrm{c}}^{-}} (\delta\mathbf{u}^{-})^{\mathrm{T}} \boldsymbol{\tau}_{\mathrm{c}}^{-} \,\mathrm{d}\Gamma = 0. \tag{7}$$

From equilibrium, we have $\boldsymbol{\tau}_{\mathrm{N}}^{+} = -\boldsymbol{\tau}_{\mathrm{N}}^{-} = \boldsymbol{\tau}_{\mathrm{N}}$ and $\boldsymbol{\tau}_{\mathrm{c}}^{+} = -\boldsymbol{\tau}_{\mathrm{c}}^{-} = \boldsymbol{\tau}_{\mathrm{c}}$. Under the assumption of infinitesimal deformation, we can write $\Gamma_{\mathrm{c}} \approx \Gamma_{\mathrm{c}}^{+} \approx \Gamma_{\mathrm{c}}^{-}$. We can also define the variation of displacement jump over the crack as $\delta\mathbf{w} = \delta\mathbf{u}^{+} - \delta\mathbf{u}^{-}$. Therefore, Eq. (7) yields

$$\int_{\Gamma_{\mathrm{c}}} \delta\mathbf{w}^{\mathrm{T}} \boldsymbol{\tau}_{\mathrm{N}} \,\mathrm{d}\Gamma + \int_{\Gamma_{\mathrm{c}}} \delta\mathbf{w}^{\mathrm{T}} \boldsymbol{\tau}_{\mathrm{c}} \,\mathrm{d}\Gamma = 0. \tag{8}$$

Based on Eq. (8), the next section presents the Finite Element implementation of a standard cohesive element and the following section proposes a novel formulation suitable for introducing pressure loading on the crack faces.

2.4. Standard cohesive element for the modelling of fracture

Consider the 2D cohesive element shown in Fig. 4(a). The element has 4 nodes, labelled 1 to 4. Each node i has nodal displacements, $\hat{\mathbf{u}}_i^{\mathrm{T}} = [\hat{u}_i, \hat{v}_i]$, which are used to compose the DoF vector for the element $\hat{\mathbf{u}}^{\mathrm{T}} = [\hat{\mathbf{u}}_1^{\mathrm{T}}, \hat{\mathbf{u}}_2^{\mathrm{T}}, \hat{\mathbf{u}}_3^{\mathrm{T}}, \hat{\mathbf{u}}_4^{\mathrm{T}}]$. The displacement jumps between pairs of corresponding nodes can be defined as $\hat{\mathbf{w}}_{14}^{\mathrm{T}} = \hat{\mathbf{u}}_4^{\mathrm{T}} - \hat{\mathbf{u}}_1^{\mathrm{T}}$ and $\hat{\mathbf{w}}_{23}^{\mathrm{T}} = \hat{\mathbf{u}}_3^{\mathrm{T}} - \hat{\mathbf{u}}_2^{\mathrm{T}}$. Finally, the vector of displacement jumps can be defined as $\hat{\mathbf{w}}^{\mathrm{T}} = [\hat{\mathbf{w}}_{14}^{\mathrm{T}}, \hat{\mathbf{w}}_{23}^{\mathrm{T}}]$. The cohesive element has a local and global coordinate system as shown in Fig. 4(a), and a natural coordinate system as shown in Fig. 4(b). The separations over the cohesive element can be given as

$$\mathbf{w} = \mathbf{N}_{\mathrm{c}} \hat{\mathbf{u}}. \tag{9}$$

where $\mathbf{N}_{\mathrm{c}}$ is the shape function matrix that correlates displacements to cohesive separations. $\mathbf{N}_{\mathrm{c}}$ can be given as [51]

$$\mathbf{N}_{\mathrm{c}} = \begin{bmatrix} -CN_1 & -SN_1 & -CN_2 & -SN_2 & CN_2 & SN_2 & CN_1 & SN_1 \\ SN_1 & -CN_1 & SN_2 & -CN_2 & -SN_2 & CN_2 & -SN_1 & CN_1 \end{bmatrix}, \tag{10}$$

where $N_1 = (1-\xi)/2$ and $N_2 = (1+\xi)/2$ with ξ denoting the natural coordinate (see Fig. 4(b)). C and S represent $\cos\theta$ and $\sin\theta$, respectively, where θ is the angle between the global and the local coordinates (see Fig. 4(a)).

Substituting Eq. (9) in Eq. (8), we get

$$\delta\hat{\mathbf{u}}^{\mathrm{T}} \left(\int_{\Gamma_{\mathrm{N}}^{e}} \mathbf{N}_{\mathrm{c}}^{\mathrm{T}} \boldsymbol{\tau}_{\mathrm{N}} \,\mathrm{d}\Gamma + \int_{\Gamma_{\mathrm{c}}^{e}} \mathbf{N}_{\mathrm{c}}^{\mathrm{T}} \boldsymbol{\tau}_{\mathrm{c}} \,\mathrm{d}\Gamma \right) = 0. \tag{11}$$

Since $\delta\hat{\mathbf{u}}$ is generic, we have

$$\int_{\Gamma_{\mathrm{N}}^{e}} \mathbf{N}_{\mathrm{c}}^{\mathrm{T}} \boldsymbol{\tau}_{\mathrm{N}} \,\mathrm{d}\Gamma + \int_{\Gamma_{\mathrm{c}}^{e}} \mathbf{N}_{\mathrm{c}}^{\mathrm{T}} \boldsymbol{\tau}_{\mathrm{c}} \,\mathrm{d}\Gamma = \mathbf{0}. \tag{12}$$

The cohesive traction $\boldsymbol{\tau}_{\mathrm{c}}$ in Eq. (12) can be expressed as

$$\boldsymbol{\tau}_{\mathrm{c}} = \mathbf{D}_{\mathrm{c}} \mathbf{w} = \mathbf{D}_{\mathrm{c}} \mathbf{N}_{\mathrm{c}} \hat{\mathbf{u}}, \tag{13}$$

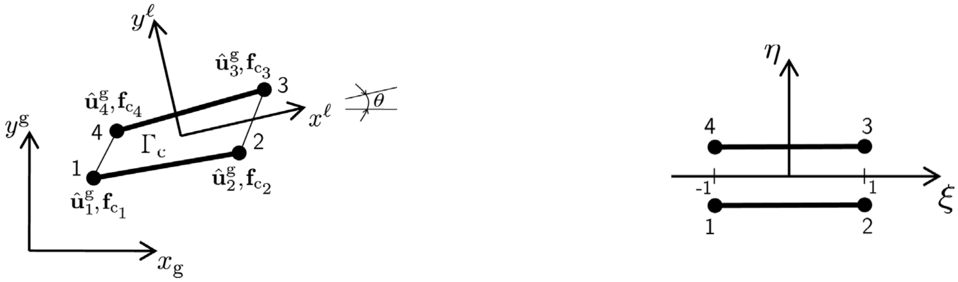

(a) Global and local coordinates.

(b) Natural coordinate.

Fig. 4. Cohesive element with 4 nodes.

where $\mathbf{D}_{\mathrm{c}}$ is the constitutive relation between the separation and tractions. Substituting Eq. (13) into Eq. (12), we get

$$\int_{\Gamma_{\mathrm{N}}} \mathbf{N}_{\mathrm{c}}^{\mathrm{T}} \boldsymbol{\tau}_{\mathrm{N}} \, \mathrm{d}\Gamma + \int_{\Gamma_{\mathrm{c}}} \mathbf{N}_{\mathrm{c}}^{\mathrm{T}} \mathbf{D}_{\mathrm{c}} \mathbf{N}_{\mathrm{c}} \, \mathrm{d}\Gamma \, \hat{\mathbf{u}} = \mathbf{0}. \tag{14}$$

Thus, the discrete equilibrium equations for the cohesive element becomes

$$\mathbf{K}_{\mathrm{c}} \hat{\mathbf{u}} = \mathbf{f}_{\mathrm{N}}, \tag{15}$$

where cohesive secant stiffness $\mathbf{K}_{\mathrm{c}}$ is defined as

$$\mathbf{K}_{\mathrm{c}} = \int_{\Gamma_{\mathrm{c}}} \mathbf{N}_{\mathrm{c}}^{\mathrm{T}} \mathbf{D}_{\mathrm{c}} \mathbf{N}_{\mathrm{c}} \, \mathrm{d}\Gamma, \tag{16}$$

and the external force vector of the cohesive element is given as

$$\mathbf{f}_{\mathrm{N}} = \int_{\Gamma_{\mathrm{N}}} \mathbf{N}_{\mathrm{c}}^{\mathrm{T}} \boldsymbol{\tau}_{\mathrm{N}} \, \mathrm{d}\Gamma. \tag{17}$$

3. A new adaptive element for damage surface loading — *pressure* elements

3.1. Introduction

Consider the case where fluid pressure is known inside a fracture in an elastic medium. To model this system, the pressure inside the crack needs to be applied to the crack surfaces. The surfaces of the crack can move as a result of the crack propagation during the numerical analysis, and their position is therefore not known a priori. In this case, an adaptive and versatile methodology to apply evolving pressure to the surfaces of a crack is needed to accurately model the damage. This can be achieved by a new element type called *pressure* element which has the capability to exert fluid pressure onto the crack surfaces in an adaptive manner and model the cohesive behaviour of the medium. The integration of this element inside the FNM numerical framework can be achieved as in standard cohesive elements and as a result, such fluid driven crack propagation problems can be handled effectively. This element type constitutes the first step towards developing the *pressure* element which will have the capability to model the fluid physics and the associated strong coupling problem.

3.2. Formulation

To account for the effect of fluid pressure acting on a solid body, an element with the same topology as the cohesive element in Fig. 4 can be formulated (see Fig. 5). Considering the equilibrium equation given in Eq. (15) for the cohesive element formulation, additional pressure forces $\mathbf{f}_{\mathrm{p}}$ with corresponding tractions $\boldsymbol{\tau}^{\mathrm{p}}$ can be acting on the crack surfaces different from the other external forces $\mathbf{f}_{\mathrm{N}}$. Then, the equilibrium equation for the this case can be written as

$$\mathbf{K}_{\mathrm{c}} \hat{\mathbf{u}} = \mathbf{f}_{\mathrm{p}} + \mathbf{f}_{\mathrm{N}}, \tag{18}$$

where the external force vector of the *pressure* element that acts on the crack surfaces can be written as

$$\mathbf{f}_{\mathrm{p}} = \int_{\Gamma_{\mathrm{N}}} \mathbf{N}_{\mathrm{c}}^{\mathrm{T}} \boldsymbol{\tau}^{\mathrm{p}} \, \mathrm{d}\Gamma. \tag{19}$$

The stiffness matrix $\mathbf{K}_{\mathrm{c}}$ represents the cohesive behaviour of the crack in the medium. If the cohesive behaviour is not introduced, then the constitutive matrix in the cohesive part becomes zero; in this case, the stiffness matrix would not contribute to the FE system but the element would still enable evolving pressure loading of the crack surfaces. A verification of this element is demonstrated in Section 6.

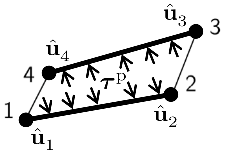

Fig. 5. Element schematic that contains applied pressure.

4. Application of *pressure* elements for multi-physics fracture problems

4.1. Hydraulic fracture theory

In hydraulic fracture problems, cracks propagate within a solid domain due to the injected fluid inside the fracture (Fig. 6). Fig. 6 shows a crack in solid medium, Ω, propagating along a curvilinear coordinate s. An incompressible fluid with viscosity μ is injected with a rate $q_0(t)$ (area per unit time). At each coordinate s inside the crack, the flow rate is $q(s,t)$, the pressure is $p(s,t)$, and the opening of the crack is $w_{\mathbf{n}}(s,t)$; i.e. $w_{\mathbf{n}} = \mathbf{n}^{\mathrm{T}} \cdot (\mathbf{u}^+ - \mathbf{u}^-)$ where $\mathbf{n}$ is the normal to the crack, $\mathbf{u}^+$ is the displacement at the upper surface and $\mathbf{u}^-$ is the displacement at the lower surface of the crack. We seek to define the fluid behaviour in order to find the forces that act on the crack surfaces. During the fluid injection, the elastic body can deform and the crack can propagate. The flow rate q is proportional to the pressure gradient $\frac{\partial p}{\partial s}$ via [52]

$$q = -\frac{w_{\mathbf{n}}^3}{12\mu}\frac{\partial p}{\partial s}. \tag{20}$$

Assuming incompressibility, the local mass conservation of the fluid can be expressed as [17]

$$\frac{\partial w_{\mathbf{n}}}{\partial t} + \frac{\partial q}{\partial s} = 0, \tag{21}$$

where t is the time. Then, combining Eqs. (20) and (21), the strong form of the fluid flow equation becomes

$$\frac{\partial w_{\mathbf{n}}}{\partial t} = \frac{\partial}{\partial s}(\frac{w_{\mathbf{n}}^3}{12\mu}\frac{\partial p}{\partial s}). \tag{22}$$

At the crack tip, $s = \ell$, the flow rate and the pressure are zero. The boundary conditions therefore can be written as

$$q(0,t) = q_0(t), \quad q(\ell,t) = 0, \quad w_{\mathbf{n}}(\ell,t) = 0, \quad p(\ell,t) = 0, \quad v_{\mathbf{n}}(s,t) = 0, \tag{23}$$

where $v_{\mathbf{n}}$ is the mid-plane displacements of the hydraulic fracture elements in the normal direction. The initial conditions can be written as

$$w_{\mathbf{n}}(s,0) = w_0(s). \tag{24}$$

Using Eq. (21), we can obtain an overall expression for the mass conservation:

$$\int_0^{\ell} \left[w_{\mathbf{n}}(s,t) - w_0(s)\right] \mathrm{d}s = \int_0^t q_0(t)\,\mathrm{d}t. \tag{25}$$

The current study focuses on a propagation regime with the provided boundary conditions as explained and formulated in this Section 4 to demonstrate the new capabilities of the proposed numerical framework. Other propagation regimes with different assumptions and idealizations can also be modelled with appropriate modifications on the proposed framework by imposing either new DoFs, Multi-Point Constraints, forces (due to the flux) or refinement schemes. Such investigations are left in the scope of future studies that utilize this framework. Here, we have applied the framework to this case to demonstrate its applicability.

4.2. Weak form of the lubrication equation

Using virtual pressures δp, the weak form of the fluid flow equation (Eq. (22)) can be formulated for 1D finite element implementation as

$$\int_{\Gamma} \delta p(\frac{\partial w_{\mathbf{n}}}{\partial t} - \frac{\partial}{\partial s}(\frac{w_{\mathbf{n}}^3}{12\mu}\frac{\partial p}{\partial s}))\,\mathrm{d}s = 0. \tag{26}$$

Applying integration by parts and rearranging the terms, we get

$$\int_{\Gamma} \frac{\partial(\delta p)}{\partial s}\frac{w_{\mathbf{n}}^3}{12\mu}\frac{\partial p}{\partial s}\,\mathrm{d}s = (\delta p\frac{w_{\mathbf{n}}^3}{12\mu}\frac{\partial p}{\partial s})|_0^{\ell} - \int_{\Gamma} \delta p\frac{\partial w_{\mathbf{n}}}{\partial t}\,\mathrm{d}s. \tag{27}$$

Substituting the boundary conditions to Eq. (27), we have

$$\int_{\Gamma} \frac{\partial(\delta p)}{\partial s}\frac{w_{\mathbf{n}}^3}{12\mu}\frac{\partial p}{\partial s}\,\mathrm{d}s = \delta p q\,|_0^{\ell} - \int_{\Gamma} \delta p\frac{\partial w_{\mathbf{n}}}{\partial t}\,\mathrm{d}s. \tag{28}$$

Using Eq. (28), the FE discretization can be implemented.

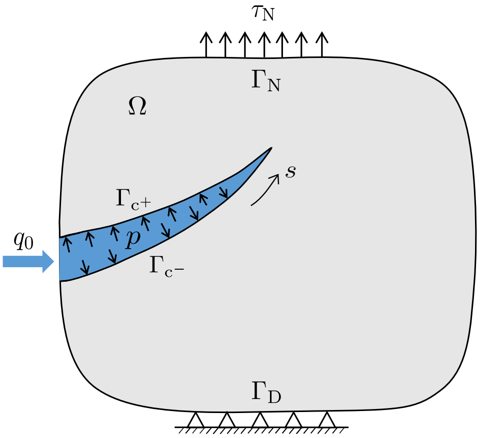

Fig. 6. 2D medium with a hydraulic fracture.

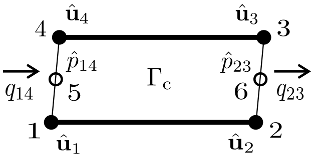

Fig. 7. Element schematic that contains pressures DoFs.

4.3. Extended formulation of pressure elements for multi-physics fluid–solid interaction problems

To model the solid and fluid behaviour concurrently, a new hydraulic fracture element can be formulated with similar topology to the previously-presented cohesive element (Fig. 4(a)), but which contains additional pressure DoFs (see Fig. 7). The element has 4 nodes labelled 1 to 4. Each one of the four nodes i has nodal displacements, $\hat{\mathbf{u}}_i^{\mathrm{T}} = [\hat{u}_i, \hat{v}_i]$, which are used to compose the displacement DoF vector for the element, $\hat{\mathbf{u}}^{\mathrm{T}} = [\hat{\mathbf{u}}_1^{\mathrm{T}}, \hat{\mathbf{u}}_2^{\mathrm{T}}, \hat{\mathbf{u}}_3^{\mathrm{T}}, \hat{\mathbf{u}}_4^{\mathrm{T}}]$. In addition, there are two nodal pressures which are used to compose the pressure DoF vector for the element, $\hat{\mathbf{p}}^{\mathrm{T}} = [\hat{p}_{14}, \hat{p}_{23}]$.

Similar to the cohesive element, the weak formulation for this element can be formulated by considering opening widths instead of displacement jumps and pressures instead of cohesive tractions. As the pressures inside the element act in the normal direction, the element will be in equilibrium with the external tractions in the normal direction $\tau_{\mathbf{n}}$. Then, using Eq. (14), the weak formulation for this element can be written as

$$\int_{\Gamma_{\mathrm{c}}} \delta w_{\mathbf{n}} \tau_{\mathbf{n}} \, \mathrm{d}\Gamma + \int_{\Gamma_{\mathrm{c}}} \delta w_{\mathbf{n}} p \, \mathrm{d}\Gamma = 0. \tag{29}$$

To find the opening width $w_{\mathbf{n}}$ using the nodal displacement DoFs, only the normal contribution of the global displacement jump matrix $\mathbf{N}_{\mathrm{c}}$ is considered. Thus, the FE approximation for the opening width can be written as

$$w_{\mathbf{n}} = \mathbf{N}_{\mathbf{n}} \hat{\mathbf{u}}, \tag{30}$$

where $\mathbf{N}_{\mathbf{n}}$ is the corresponding shape function given as (from Eq. (10))

$$\mathbf{N}_{\mathbf{n}} = \begin{bmatrix} SN_1 & -CN_1 & SN_2 & -CN_2 & -SN_2 & CN_2 & -SN_1 & CN_1 \end{bmatrix}. \tag{31}$$

The 1D pressure field inside the element can be discretized using a suitable shape function matrix $\mathbf{N}_p$:

$$p = \mathbf{N}_p \hat{\mathbf{p}}, \text{ with} \tag{32}$$

$$\mathbf{N}_p = \begin{bmatrix} N_1 & N_2 \end{bmatrix}. \tag{33}$$

Substituting Eqs. (30) and (32) in Eq. (29), we obtain

$$\delta \hat{\mathbf{u}}^{\mathrm{T}} \left(\int_{\Gamma_{\mathrm{c}}} \mathbf{N}_{\mathbf{n}}^{\mathrm{T}} \tau_{\mathbf{n}} \, \mathrm{d}\Gamma + \int_{\Gamma_{\mathrm{c}}} (\mathbf{N}_{\mathbf{n}})^{\mathrm{T}} \mathbf{N}_p \, \mathrm{d}\Gamma \, \hat{\mathbf{p}} \right) = 0. \tag{34}$$

Then, Eq. (34) can be written in the following form:

$$-\mathbf{Q}\hat{\mathbf{p}} = \mathbf{f}_{\mathrm{N}}, \tag{35}$$

where $\mathbf{Q}$ is the coupling matrix between the fluid and solid parts and is given as

$$\mathbf{Q} = \int_{\Gamma_\mathrm{c}} \mathbf{N}_\mathbf{n}^\mathrm{T}\mathbf{N}_p \,\mathrm{d}\Gamma, \tag{36}$$

and $\mathbf{f}_\mathrm{N}$ is the external force vector corresponding to the Neumann boundary conditions:

$$\mathbf{f}_\mathrm{N} = \int_{\Gamma_\mathrm{c}} \mathbf{N}_\mathbf{n}^\mathrm{T}\tau_\mathbf{n} \,\mathrm{d}\Gamma. \tag{37}$$

Using the weak form of the lubrication equation (Eq. (28)), but applying it now to a single element (Fig. 7), we get

$$\int_{\Gamma_\mathrm{c}} \frac{\partial(\delta p)}{\partial s}\frac{w_\mathbf{n}^3}{12\mu}\frac{\partial p}{\partial s}\,\mathrm{d}s = \delta p q \,|_{\xi_1}^{\xi_2} - \int_{\Gamma_\mathrm{c}} \delta p \frac{\partial w_\mathbf{n}}{\partial t}\,\mathrm{d}s, \tag{38}$$

where $\xi_1 = -1$ and $\xi_2 = 1$ following Fig. 4(b). Substituting Eq. (32) to the weak formulation of the fluid part (Eq. (38)), we have

$$\delta\hat{\mathbf{p}}^\mathrm{T}\left(\int_{\Gamma_\mathrm{c}} \mathbf{N}_p^\mathrm{T}\frac{\partial w_\mathbf{n}}{\partial t}\,\mathrm{d}s - \mathbf{N}_p^\mathrm{T} q \,|_{\xi_1}^{\xi_2} + \int_{\Gamma_\mathrm{c}} \frac{\partial \mathbf{N}_p^\mathrm{T}}{\partial s}\frac{w_\mathbf{n}^3}{12\mu}\frac{\partial \mathbf{N}_p}{\partial s}\,\mathrm{d}s\,\hat{\mathbf{p}}\right) = \mathbf{0}. \tag{39}$$

Then, substituting Eq. (30) into Eq. (39), we obtain

$$\int_{\Gamma_\mathrm{c}} \mathbf{N}_p^\mathrm{T}\mathbf{N}_\mathbf{n}\dot{\hat{\mathbf{u}}}\,\mathrm{d}s + \int_{\Gamma_\mathrm{c}} \frac{\partial \mathbf{N}_p^\mathrm{T}}{\partial s}\frac{w_\mathbf{n}^3}{12\mu}\frac{\partial \mathbf{N}_p}{\partial s}\,\mathrm{d}s\,\hat{\mathbf{p}} = \mathbf{N}_p^\mathrm{T} q \,|_{\xi_1}^{\xi_2} = \mathbf{f}_q, \tag{40}$$

where $\dot{\hat{\mathbf{u}}}$ represents the nodal vector for time derivative of the displacements. We have also defined $\mathbf{f}_q = \mathbf{N}_p^\mathrm{T} q \,|_{\xi_1}^{\xi_2}$. Then, Eq. (40) can be written in the following form:

$$\mathbf{Q}^\mathrm{T}\dot{\hat{\mathbf{u}}} + \mathbf{H}\hat{\mathbf{p}} = \mathbf{f}_q, \tag{41}$$

where $\mathbf{Q}^\mathrm{T}$ is the transpose of the coupling matrix

$$\mathbf{Q}^\mathrm{T} = \int_{\Gamma_\mathrm{c}} \mathbf{N}_p^\mathrm{T}\mathbf{N}_\mathbf{n} \,\mathrm{d}\Gamma, \tag{42}$$

and $\mathbf{H}$ is the stiffness matrix for the fluid part of the element given as

$$\mathbf{H} = \int_{\Gamma_\mathrm{c}} \frac{\partial \mathbf{N}_p^\mathrm{T}}{\partial s}\frac{w_\mathbf{n}^3}{12\mu}\frac{\partial \mathbf{N}_p}{\partial s}\,\mathrm{d}s. \tag{43}$$

Then, assembling the element matrices of fluid and solid parts, the discrete governing equations can be formulated as

$$\begin{bmatrix}\mathbf{0} & \mathbf{0}\\ \mathbf{Q}^\mathrm{T} & \mathbf{0}\end{bmatrix}\begin{pmatrix}\dot{\hat{\mathbf{u}}}\\ \dot{\hat{\mathbf{p}}}\end{pmatrix} + \begin{bmatrix}\mathbf{0} & -\mathbf{Q}\\ \mathbf{0} & \mathbf{H}\end{bmatrix}\begin{pmatrix}\hat{\mathbf{u}}\\ \hat{\mathbf{p}}\end{pmatrix} = \begin{pmatrix}\mathbf{f}_\mathrm{N}\\ \mathbf{f}_q\end{pmatrix}. \tag{44}$$

The time derivative of the displacements $\dot{\hat{\mathbf{u}}}$ can be approximated using an implicit backwards Euler scheme as

$$\dot{\hat{\mathbf{u}}}_n = \frac{\hat{\mathbf{u}}_n - \hat{\mathbf{u}}_{n-1}}{\Delta t}, \tag{45}$$

where t refers to the time and the time increment is $\Delta t = t_n - t_{n-1}$ where n refers to the current time step. Then, inserting Eq. (45) into Eq. (44), we have

$$\begin{bmatrix}\mathbf{0} & -\mathbf{Q}\\ \mathbf{Q}^\mathrm{T} & \mathbf{H}\Delta t\end{bmatrix}\begin{pmatrix}\hat{\mathbf{u}}\\ \hat{\mathbf{p}}\end{pmatrix} = \begin{pmatrix}\mathbf{f}_\mathrm{N}\\ \mathbf{f}_q\Delta t - \mathbf{Q}^\mathrm{T}\hat{\mathbf{u}}_{n-1}\end{pmatrix}, \tag{46}$$

where the subscripts n for the variables in the current time step are omitted for simplicity. Note that Eq. (46) does not yet impose the symmetry of the crack opening.

In fact, the formulation assumes that pressure acts on the two crack surfaces in a symmetric manner. Thus, initially-coinciding surfaces of the crack open symmetrically at the nodal points. This information needs to be included in the formulation through proper multi-point constraints to impose the complete relation between the opening widths and displacements.

The symmetric opening of the initially-coinciding surfaces implies that the mid-plane does not move in the normal (opening width) direction. The normal component of the mid-plane displacement can be related to the element nodal displacement vector $\hat{\mathbf{u}}$ through the matrix $\mathbf{L}_\mathrm{m}^\mathbf{n}$ and then be set to zero:

$$\mathbf{L}_\mathrm{m}^\mathbf{n}\hat{\mathbf{u}} = 0, \tag{47}$$

with

$$\mathbf{L}_\mathrm{m}^\mathbf{n} = \frac{1}{2}\begin{bmatrix}-SN_1 & CN_1 & -SN_2 & CN_2 & -SN_2 & CN_2 & -SN_1 & CN_1\end{bmatrix} \tag{48}$$

derived using a similar approach as $\mathbf{N}_\mathbf{n}$ that relates element nodal displacement vector to the opening width.

Using a penalty stiffness formulation, the corresponding penalty energy can be written as

$$U_\mathrm{m} = \frac{1}{2}k_\mathrm{p}(\mathbf{L}_\mathrm{m}^\mathbf{n}\hat{\mathbf{u}})\cdot(\mathbf{L}_\mathrm{m}^\mathbf{n}\hat{\mathbf{u}}) = \frac{1}{2}\hat{\mathbf{u}}^\mathrm{T}k_\mathrm{p}(\mathbf{L}_\mathrm{m}^\mathbf{n})^\mathrm{T}\mathbf{L}_\mathrm{m}^\mathbf{n}\hat{\mathbf{u}}. \tag{49}$$

The derivative with respect to the displacement DoFs $\hat{\mathbf{u}}$ lead to the stiffness matrix

$$\mathbf{K}_\mathrm{m} = k_\mathrm{p}(\mathbf{L}_\mathrm{m}^\mathbf{n})^\mathrm{T}\mathbf{L}_\mathrm{m}^\mathbf{n} \tag{50}$$

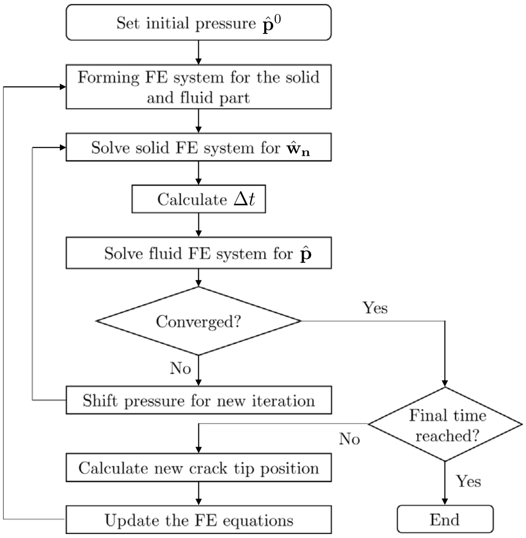

Fig. 8. Flowchart for the numerical scheme to simulate pressure-driven fracture propagation.

which can be added to the overall formulation given in Eq. (46):

$$\begin{bmatrix} \mathbf{K}_\mathrm{m} & -\mathbf{Q} \\ \mathbf{Q}^\mathrm{T} & \mathbf{H}\Delta t \end{bmatrix} \begin{pmatrix} \hat{\mathbf{u}} \\ \hat{\mathbf{p}} \end{pmatrix} = \begin{pmatrix} \mathbf{f}_\mathrm{N} \\ \mathbf{f}_q \Delta t - \mathbf{Q}^\mathrm{T}\hat{\mathbf{u}}_{n-1} \end{pmatrix}. \tag{51}$$

Using Eq. (51), a special finite element can be constructed to model the hydraulic fracture problem. The elements of this type can then be assembled together with the continuum elements in the rest of the domain using the standard FNM procedure as in the case of cohesive elements [40].

5. Numerical solution procedures

5.1. Introduction

The fluid–solid coupling problems can be solved either by iterative or simultaneous procedures. The numerical implementation of the two methodologies are presented in this section.

5.2. Iterative procedure

In order to couple the individual solid and fluid FE systems, a Picard iteration scheme (see Fig. 8) can be used [3]. For solving the structural part involving a crack as shown in Fig. 8, any appropriate method can be used such as XFEM or FNM. To implement the scheme, the time step needs to be calculated at each iteration. This can be achieved by applying time discretization to Eq. (21) and re-arranging the terms to solve for the time step Δt:

$$\Delta t = \frac{1}{q_0} \int_0^l \Delta w_\mathbf{n} \,\mathrm{d}s. \tag{52}$$

The sequence of operations used by the Picard iteration is:

$$\begin{aligned} \hat{\mathbf{p}}_{r+1/2} &= \mathbf{H}(\hat{\mathbf{w}}_n)^{-1}\mathbf{F}^\mathrm{hf}(\hat{\mathbf{w}}_n) \\ \hat{\mathbf{p}}_{r+1} &= \alpha\hat{\mathbf{p}}_{r+1/2} + (1-\alpha)\hat{\mathbf{p}}_r \\ \hat{\mathbf{u}}_{r+1} &= \mathbf{K}^{-1}\mathbf{F}^\mathrm{st}(\hat{\mathbf{p}}_{r+1}) \\ \hat{\mathbf{u}}_{r+1} &\to (\hat{\mathbf{w}}_n)_{r+1}, \end{aligned} \tag{53}$$

where r is the iteration number, α is the Picard iteration coefficient, $\mathbf{K}$ represents the stiffness matrix for the structural part and $\mathbf{F}^\mathrm{st}$ denotes the corresponding nodal force vector. The convergence of the algorithm is checked using the following criterion

$$\frac{\sum_{i=1}^{m_\mathrm{f}} \left|\hat{p}_i^{(r)} - \hat{p}_i^{(r-1)}\right|}{\sum_{i=1}^{m_\mathrm{f}} \left|\hat{p}_i^{(r)}\right|} \le \epsilon, \tag{54}$$

where ϵ is the convergence tolerance and $\hat{p}_i^{(r)}$ is the pressure at node i in iteration r. By solving the fluid part, the pressure distribution along the crack is obtained.

5.3. Simultaneous procedure

A Newton–Raphson scheme can be used to solve the hydraulic fracture system in a simultaneous fashion using the formulation given in Eq. (51). As the system is non-linear, the scheme involves calculating the stiffness matrix and the residual force for several iterations until convergence is satisfied. Since the system is also time dependent, the iterations are carried out for each time step. Thus, for a given time step and iteration, the Newton–Raphson scheme solves:

$$\begin{bmatrix} \mathbf{0} & -\mathbf{Q} \\ \mathbf{Q}^{\mathrm{T}} & \mathbf{H}\Delta t \end{bmatrix}_n^{i-1} \begin{pmatrix} \Delta\hat{\mathbf{u}} \\ \Delta\hat{\mathbf{p}} \end{pmatrix}_n^{i} = \begin{pmatrix} \mathbf{0} \\ \mathbf{f}_q \Delta t \end{pmatrix}_n - \begin{pmatrix} -\mathbf{Q}\hat{\mathbf{p}}_n^{i-1} \\ \mathbf{Q}^{\mathrm{T}}\hat{\mathbf{u}}_n^{i-1} - \mathbf{Q}^{\mathrm{T}}\hat{\mathbf{u}}_{n-1}^{i-1} + \mathbf{H}\Delta t\,\hat{\mathbf{p}}_n^{i-1} \end{pmatrix}, \tag{55}$$

where i is the iteration number and n refers to the time step. The first part of the right hand side of Eq. (55) is the external force vector whereas the second part is the internal force vector of the Newton–Raphson scheme. Notice that the only non-zero external force in this system is induced by the inlet flux as given in Eq. (44). In this scheme, the time step needs to be sufficiently small in order to attain accurate and converged solutions. By solving this system of equations, the pressure and displacement DoFs can be calculated for a certain time step.

5.4. Numerical considerations

During the implementation stage of the proposed multi-physics *pressure* element as a user-defined element, several numerical challenges have been encountered and addressed, as detailed here:

- the coupled mechanical-fluid problem has non-linearity, non-locality and time dependence —all of which make the system difficult to solve. In order to solve this system, it is formulated as a quasi-static problem by introducing the implicit backward Euler scheme for time dependence; to deal with the non-linearity, a Newton–Raphson scheme is used in the simultaneous procedure. Thus, the time step needs to be small enough for accurate predictions; the results presented here were all verified to be converged with respect to the time step.
- in the iterative procedure, the converged solutions can be attained only for certain instances in time determined by the Picard iteration scheme. When solving this system numerically, a certain crack length needs to be set due to the discretization of the model, i.e. a continuous change of the fracture length is not practical in a FE system. Thus, the DoFs can only be calculated for discrete points in time with their associated crack length.
- in the iterative model, the time increment has to be determined via the Picard iteration scheme. This effectively means that the displacements required to calculate the time derivative of the opening width are extracted using the solution of the previous crack length.
- as the iterative scheme involves solving the individual elastic and fluid FE systems multiple times for convergence, it requires significantly higher computational time than the simultaneous procedure where both are solved in a concurrent manner.

6. Verification of the *pressure* element for adaptive crack face loading

6.1. Introduction

In order to verify the *pressure* element, a case which involves calculating the stress intensity factors of a slant crack inside an infinite elastic body for different crack angles is chosen. Given the equivalence between stress intensity factors due to remote stress and due to pressure applied on the cracks faces [53], we ran two simulations: the first to obtain a benchmark solution with remote loading, and the second one using the new *pressure* elements and crack face loading.

6.2. Evaluation of stress intensity factors for a centre slant crack subject to remote and crack face loading

In this section, we calculate the SIF in mode I (K_{I}) and mode II (K_{II}) for a centre slant crack (Fig. 9(a)) with different orientations θ in a material medium with respect to remote and crack face loading [40]. The material medium is modelled as a large plate with dimensions $L = W = 10\,\mathrm{mm}$ (Fig. 9(a)). In the remote loading case, this plate is exposed to tensile stresses $\sigma = 1\,\mathrm{MPa}$ as shown in Fig. 9(a) to simulate the applied remote stress to the material medium. In the crack face loading case, instead of this tensile stress, we apply the equivalent crack face loading for different crack orientations and calculate the corresponding energy release rates.

When modelling this plate, we assume plane stress in an isotropic medium with Young's modulus and Poisson's ratio $E = 200\,\mathrm{GPa}$ and $\nu = 0.3$, respectively. The crack length is defined such that the horizontal projection of the crack stays constant with $a\cos\theta = 0.1W$ (see Fig. 9(a)). The body is discretized with 80 elements across the width and 81 elements across the height. The mesh is composed of first order quadrilateral, plane stress elements.

In the VCCT relations in Eqs. (3) and (4), here repeated for convenience,

$$G_{\mathrm{I}} = \frac{1}{2A_{\mathrm{W}}} F_{\mathrm{n}} [\![q_{\mathrm{n}}]\!] \left(\frac{A_{\mathrm{W}}}{A_{\mathrm{CT}}} \right)^{1/2} \tag{56}$$

$$G_{\mathrm{II}} = \frac{1}{2A_{\mathrm{W}}} F_{\mathrm{t}} [\![q_{\mathrm{t}}]\!] \left(\frac{A_{\mathrm{W}}}{A_{\mathrm{CT}}} \right)^{1/2}. \tag{57}$$

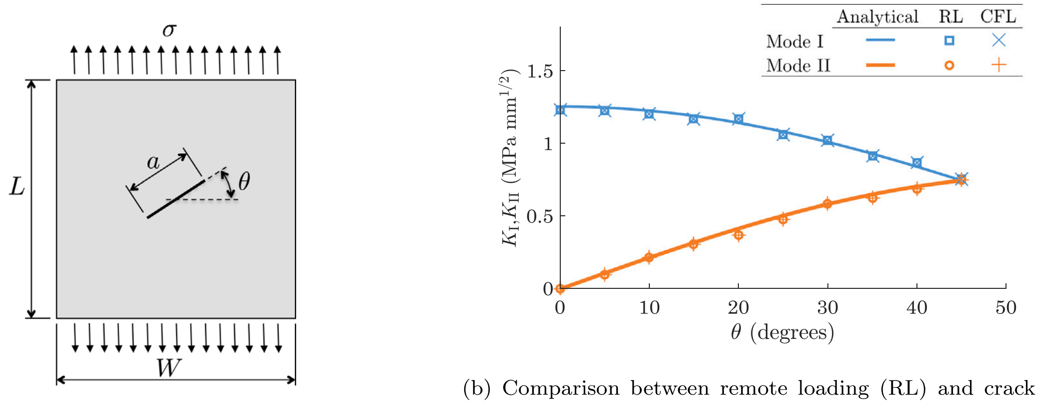

(a) Slanted crack model [40].

(b) Comparison between remote loading (RL) and crack face loading (CFL) for slant cracks.

Fig. 9. For this slant crack model, the FNM captures the SIF well in modes I and II for different angles θ.

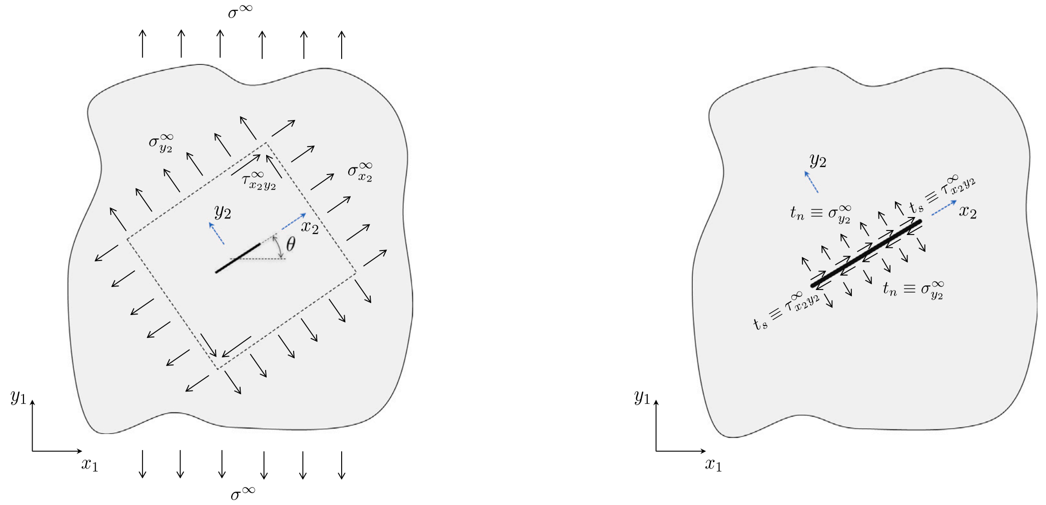

(a) Remote loading.

(b) Crack face loading.

Fig. 10. Stress state on the crack faces equivalent to the remote application of the load.

The stress intensity factors are calculated using VCCT as explained in Section 2.2.3. The energy release rates in mode I and mode II calculated using VCCT were then related to the corresponding SIFs using

$$K_{\mathrm{I}} = \sqrt{G_{\mathrm{I}} E} \tag{58}$$

$$K_{\mathrm{II}} = \sqrt{G_{\mathrm{II}} E}. \tag{59}$$

The FNM predictions for remote loading case (RL) presented in Fig. 9(b) show good agreement with the analytical solutions for different orientations of the crack.

To verify the *pressure* element, this slant crack example is chosen. However, instead of applying remote loading, equivalent crack face loading is applied to the elastic body using the *pressure* elements and the corresponding stress intensity factors are calculated for comparison.

According to fracture mechanics, SIFs are equal when equivalent boundary conditions are applied remotely or onto the crack faces. In the slant crack example, the same SIFs are obtained when a remote stress is applied (Fig. 10(a)) and when τ_{n} and τ_{s} are applied to the crack faces (Fig. 10(b)) provided

$$\tau_{\mathrm{n}} = \sigma^\infty_{\mathrm{y}_2} = \sigma^\infty \cos^2\theta, \tag{60}$$

$$\tau_{\mathrm{s}} = \tau^\infty_{\mathrm{x}_2\mathrm{y}_2} = -\sigma^\infty \cos\theta \sin\theta. \tag{61}$$

In order to calculate SIFs using VCCT considering crack face loading, the initial formulation needs to be modified. In addition to the forces at the crack tip needed for the VCCT, the contribution of the tractions $\boldsymbol{\tau}^{\mathrm{p}} = [\tau_{\mathrm{n}}\ \tau_{\mathrm{s}}]^{\mathrm{T}}$ applied by the fluid onto the crack faces around the crack tip region Γ_{ct} needs to be included in the fracture energy calculation. This region corresponds to the half length between the nodes adjacent to the crack tip along fracture plane $((\ell_{\mathrm{W}} + \ell_{\mathrm{CT}})/2)$. Then, the applied tractions $\boldsymbol{\tau}^{\mathrm{p}}$ lead to the nodal forces

$$\mathbf{F}^{\mathrm{p}} = \int_{\Gamma_{\mathrm{ct}}} \mathbf{N}^{\mathrm{T}} \boldsymbol{\tau}^{\mathrm{p}}\, \mathrm{d}\Gamma \tag{62}$$

where $\mathbf{N}$ represents standard matrix of shape functions. These forces $\mathbf{F}^{\mathrm{p}}$ due to the fluid pressure can be separated in normal $F_{\mathrm{n}}^{\mathrm{p}}$ and tangential $F_{\mathrm{t}}^{\mathrm{p}}$ components as $\mathbf{F}^{\mathrm{p}} = \left[F_{\mathrm{n}}^{\mathrm{p}}\ F_{\mathrm{t}}^{\mathrm{p}}\right]^{\mathrm{T}}$. The energy release rate calculation from VCCT then becomes

$$G_{\mathrm{I}} = \frac{1}{2A_{\mathrm{W}}}(F_{\mathrm{n}} + F_{\mathrm{n}}^{\mathrm{p}})[\![q_{\mathrm{n}}]\!]\left(\frac{A_{\mathrm{W}}}{A_{\mathrm{CT}}}\right)^{1/2} \tag{63}$$

$$G_{\mathrm{II}} = \frac{1}{2A_{\mathrm{W}}}(F_{\mathrm{t}} + F_{\mathrm{t}}^{\mathrm{p}})[\![q_{\mathrm{t}}]\!]\left(\frac{A_{\mathrm{W}}}{A_{\mathrm{CT}}}\right)^{1/2}. \tag{64}$$

Using Eqs. (63) and (64), the VCCT calculations in the case of crack face loading can be performed.

Fig. 9(b) shows that the SIF results for the case of crack face loading match exactly with the SIF results of the remote loading. This example demonstrates that accurate prediction of the SIFs can be achieved using the proposed *pressure* element which can successfully apply hydraulic loads onto crack faces inside an elastic medium.

7. Verification and application of the *pressure* element for multi-physics problems

7.1. Introduction

In order to verify the coupling problem in hydraulic fracture, the Kristianovic-Geerstma-de Klerk (KGD) model [54] is used. This model simulates the propagation of an edge-crack driven by a pressurized fluid inside it, in an infinite elastic medium (Fig. 6). The fluid is assumed to have uniform pressure in the cross section perpendicular to the crack direction, and its distribution along the fracture is dictated by the Newtonian flow resistance in a narrow channel. The KGD model [54] that we use assumes rectangular shape through the thickness. Furthermore, this model also assumes that the viscous energy of the fluid is much greater than the fracture energy required to propagate the crack. This effectively means that the fracture length does not depend on the fracture toughness. The elastic medium is isotropic and assumed to be under plane strain conditions.

In these conditions, the corresponding analytical formulation for the fracture length ℓ, opening width $w_{\mathbf{n}}$ and pressure p at the inlet in terms of Young's modulus E, Poisson's ratio ν, the inlet flux q_0, viscosity μ and time t can be given as [55]

$$\ell(t) = 0.576\left[\frac{E\, q_0^3}{\mu(1-\nu^2)}\right]^{1/6} t^{2/3} \tag{65}$$

$$w_{\mathbf{n}}(0,t) = 2.425\left[\frac{\mu\, q_0^3\,(1-\nu^2)}{E}\right]^{1/6} t^{1/3} \tag{66}$$

$$p(0,t) = 1.246\left[\frac{\mu\, E^2}{(1-\nu^2)^2}\right]^{1/3} t^{-1/3}. \tag{67}$$

7.2. Numerical model

The numerical model is composed of a 2D continuum mesh with an edge crack as shown in Fig. 11. The mesh dimensions and boundary conditions were chosen such that the model can approximate an infinite medium, and a model size parametric study was carried out to verify this. The mesh is composed of plane strain quadrilateral elements with linear shape functions. The dimensions of each element is chosen as 40 mm × 40 mm around the crack region. Following Wu et al. [3], isotropic material properties are assigned to the solid body with Young's modulus and Poisson's ratio being 30 GPa and 0.2, respectively; the fluid has viscosity of 0.1 Pa·s with the inlet flux (pump rate) of 0.001 m^2/s.

An edge crack with an initial length of 400 mm is placed to the centre left of the mesh using FNM. This problem was simulated using both the iterative (Section 5.2) and simultaneous (Section 5.3) procedures presented previously.

7.3. Results

The numerical model is simulated to find the change of the opening width, pressure and fracture length at the fracture inlet in time. These results are provided in Figs. 12(a), 12(b) and 12(c) for both the iterative and simultaneous procedures together with the corresponding analytical solution (Eqs. (65)–(67)) and a numerical solution from Wang et al. [3].

In Figs. 13(a) and 13(b), the opening width and pressure profile along the fracture length at different time instances are shown. The elliptic crack profile and its growth as it progresses in time and space can be observed together with the corresponding pressure profile.

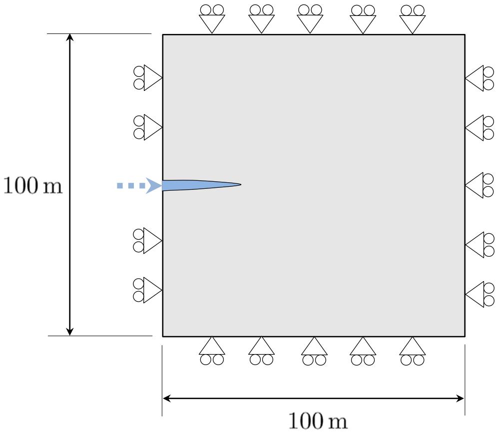

Fig. 11. Geometry and schematic of the problem.

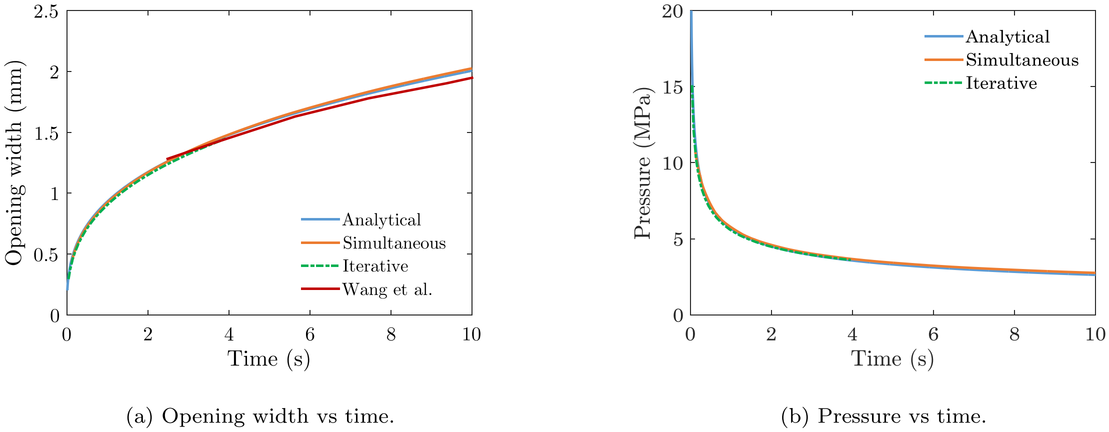

(a) Opening width vs time.

(b) Pressure vs time.

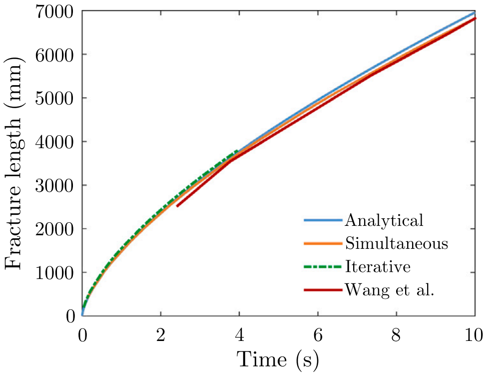

(c) Fracture length vs time.

Fig. 12. Simulation results with respect to time at the fracture inlet, compared against analytical (Eqs. (65), (66) and (67) [55]) and numerical [3] results.

7.4. Discussion

In Figs. 12(a), 12(b) and 12(c), the analytical solutions are well captured by the present approach for both iterative and simultaneous procedures. When we compare the iterative and simultaneous solutions in Figs. 12(a), 12(b) and 12(c), we observe that they match each other well. The small difference between the two can be attributed to the difference in the solution scheme: in the iterative case, the time increment that is used to calculate the time derivative of the opening width is dictated by the Picard

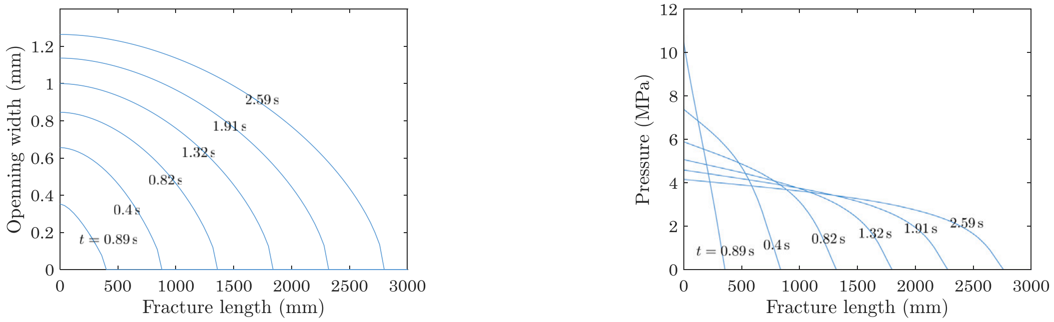

(a) Opening distribution.

(b) Pressure distribution.

Fig. 13. Opening width and pressure distribution along the fracture length together with the corresponding time t.

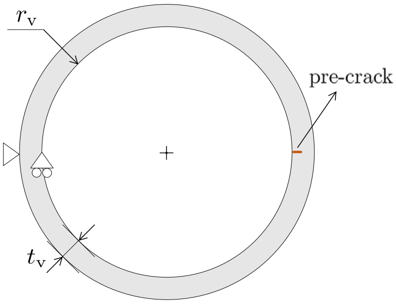

Fig. 14. Pressure vessel model in 2D with pre-crack.

iteration. Smaller time steps that would increase the accuracy in the solution cannot be applied directly; this is not the case in the simultaneous procedure where the smaller time increments can be imposed directly. Nonetheless, we observe that both sets of results compare well. This is due to the fact that the fracture length increment for each propagation of the crack is sufficiently small to provide small time steps. As the time step is determined by the Picard iteration scheme and the fracture length, small fracture lengths lead to smaller time steps.

Figs. 13(a) and 13(b) show the progression of the opening width and the pressure profiles in a hydraulic fracture process. The general shape of the opening width and pressure profiles are retained throughout the simulation which is consistent with literature [3,55]. The simultaneous procedure requires significantly less computational time than the iterative procedure (about 22%) as the elastic and fluid parts are solved concurrently.

We infer from all the above that this new framework offers a versatile platform whereby coupled multi-physics problems can be modelled in a practical manner with the capability to account physical discontinuities in their exact location and achieve coupling at element level without resorting to remeshing.

8. Application to a crack propagation problem in a pressure vessel using VCCT

8.1. Introduction

In order to further test the proposed element for a case that involves crack propagation in a structure, a pressure vessel with a pre-crack is simulated. A schematic for the test case is provided in Fig. 14. We assume that there are no variations along the length of the pressure vessel. A pre-crack is introduced to the inner middle right section of the vessel as shown in Fig. 14. In this example, VCCT-based crack propagation is followed (see Section 2.2.3). Upon pressure loading, the propagation of the crack is analysed and the critical loads of propagation for different crack lengths are compared against the analytical solutions.

The analytical solution for this case can be derived using the formulation for the stress intensity factor at the crack tip K_I of a single-edge cracked plate under uniform far field tension stress σ^∞ [56]:

$$K_\mathrm{I} = 1.12\sigma^\infty\sqrt{\pi a}, \tag{68}$$

where a is the crack length.

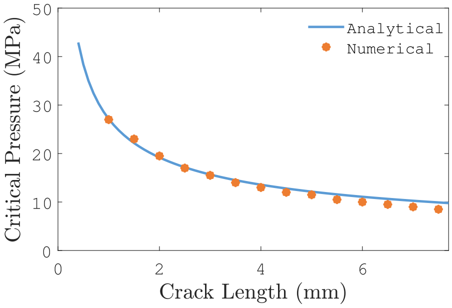

Fig. 15. Critical pressure vs. crack length.

Assuming that the crack is very small compared to the thickness of the vessel, the circumferential stress σ_v acting on the edges as a result of the pressure loading can be assumed to act as the remote load σ^∞. The circumferential stress can be calculated using the internal pressure p, the inner radius r_v and thickness t_v of the vessel as [57,58]

$$\sigma_\mathrm{v} = \frac{p(r_\mathrm{v} + t_\mathrm{v})}{t_\mathrm{v}}. \tag{69}$$

The pressure loading on the crack faces can also be treated as a remote loading as discussed in Section 6.2. Thus, the total remote loading σ^∞ can be given as

$$\sigma^\infty = \frac{p(r_\mathrm{v} + t_\mathrm{v})}{t_\mathrm{v}} + p = \frac{p(r_\mathrm{v} + 2t_\mathrm{v})}{t_\mathrm{v}}. \tag{70}$$

Then, the critical pressure for crack propagation p_c becomes

$$p_\mathrm{c} = \frac{K_\mathrm{I} t_\mathrm{v}}{1.12(r_\mathrm{v} + 2t_\mathrm{v})\sqrt{\pi a}}. \tag{71}$$

8.2. Numerical model

The model dimensions i.e. the inner radius r_v and the thickness t_v of the vessel are 40 mm and 1000 mm, respectively. For the numerical model, a 2D mesh is constructed corresponding to the model geometry (see Fig. 14) composed of plane strain quadrilateral elements with linear shape functions. A sufficiently refined, converged mesh is used to capture the stress state of the system adequately. The elements have approximately 0.5×0.5 mm size which can vary depending on the position of the element (0.5 mm is used for the mesh seeding on edges).

An isotropic material is assigned to the continuum mesh with Young's Modulus, energy release rate (Mode-I) and Poison's ratio 200 GPa, 1455 kJ/m^2 and 0.3, respectively. The crack experiences Mode-I loading due to the applied pressures. The boundary conditions are also shown in Fig. 14. They are imposed such that the clamping of the vessel to the surroundings are adequately simulated.

To impose the pressure on the inner surfaces of the vessel, we calculate the corresponding loads for each element along the vessel inner surface and apply them perpendicularly to the inner-most nodes of these elements. To apply the same vessel pressure to the crack surfaces during the implementation, this pressure is stored in a global variable and then used to apply the corresponding loads inside the *pressure* elements.

8.3. Results and discussion

The critical loads (where energy release rate is critical) for different crack lengths are provided in Fig. 15. As expected, the critical load decreases with increased crack length. The results compare well with the analytical formulation (Eq. (71)). This demonstrates that the elements can handle pressure application in practical manner on the crack surfaces for problems that has industrial relevance.

The difference between the numerical and analytical solutions at the latter stages of crack propagation can be attributed to the fact that the assumption made in the analytical formulation regarding the relative scales of the elastic medium and the crack does hold less and less as the crack grows.

9. Modelling multi-damage failure of composite pressure vessel using adaptive *pressure* elements

9.1. Introduction

The proposed numerical framework's capabilities are further investigated in another application case (Fig. 16) involving failure of pressurized composite vessels with high number of cracking and delamination. In this application case, pressurized vessels with

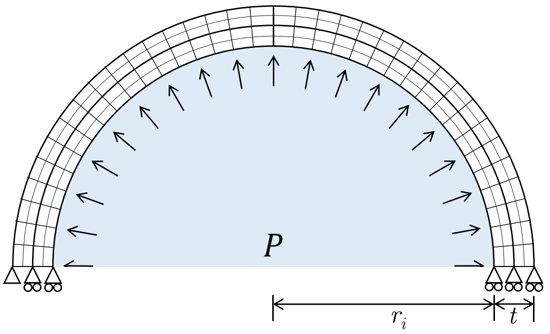

Fig. 16. 2D benchmark model for the transverse cross section of a pressure vessel.

Table 1
Geometrical dimensions of simulated vessels.

Geometrical parameters	Thin vessel (mm)	Thick vessel (mm)
Ply thickness t_p	0.5	1.0
Vessel thickness t	4.5	9.0
Vessel inner radius r_i	300.0	300.0
Vessel outer radius r_o	304.5	309.0

Table 2
Elasticity related material properties for IM7-8552 [59].

E_{11} (GPa)	$E_{22} = E_{33}$ (GPa)	$\nu_{12} = \nu_{13}$	ν_{23}	$G_{12} = G_{13}$ (GPa)	G_{23} (GPa)
161	11.38	0.32	0.44	5.17	3.98

Table 3
Fracture and strength related material properties for IM7-8552 [59,60].

G_{Ic} (kJ/m^2)	G_{IIc} (kJ/m^2)	η	Y_{n} (MPa)	Y_{t} (MPa)	S (MPa)	k (N/mm^3)
0.21	0.77	2.1	2724	60	90	10^6

different geometrical dimensions are simulated to model their failure and predict their associated burst pressure. The thickness size with respect to the vessel cross-section radius can have a strong influence on the failure and burst pressure of the vessels. Typically, analytical prediction of this relation is challenging particularly when considering extensive cracking and delamination. Thus, FEM based failure modelling with adaptive capabilities is critical to capture the complexity of curved composite structural failure. Moreover, the capability to integrate cohesive zone modelling is also critical particularly in capturing delamination along the ply interfaces and their interaction with matrix cracks. Thus, *pressure* elements with cohesive zones placed along all the ply interfaces to account for these failure mechanisms.

9.2. Numerical model

Representative schematic for this benchmark model of pressure vessel with the transverse cross-section is provided in Fig. 16. Geometrical parameters i.e. vessel inner radius r_i and thickness t are also provided together with the boundary and loading conditions. The vessels with thin and thick geometries are simulated (see Table 1). Uniform pressure loading on the inner vessel surfaces was applied. Load was sequentially increased by 0.1 MPa during the numerical analysis. The properties of the vessel composite material are provided in Tables 2 and 3. The composite vessels are composed of 9 plies and the stacking sequence is $[(90/0)_2/\bar{90}]_s$.

For effective and versatile modelling of various vessel geometries with different refinement and partitioning schemes, a higher-scale (through-the-thickness) element named the *vessel* element is developed capable of representing entire vessel thickness. This element is composed of Floating Nodes assigned to element edges and internal regions (see Fig. 17). Depending on the failure case, these nodes are activated to form various sub-elements for representing the damage inside the vessel along the thickness. Essentially, 1000 *vessel* elements are used to model the vessel circumferential/hoop direction (each having 18 continuum sub-elements along the vessel thickness (2 per each ply, see Fig. 17) resulting in overall 18 000 continuum elements in the numerical model). Different refinement schemes can be introduced with appropriate modification of the *vessel* element; here, each ply is modelled as in Fig. 18. The 2D continuum elements used to simulate the vessel medium have plane strain formulation and full-integration scheme. Along the ply interfaces and within the plies after fracture, there are *pressure* elements with cohesive zones. For these 1D *pressure* elements, Gaussian integration was used. Different topologies of this element for the failure simulation are given in Fig. 17. The element

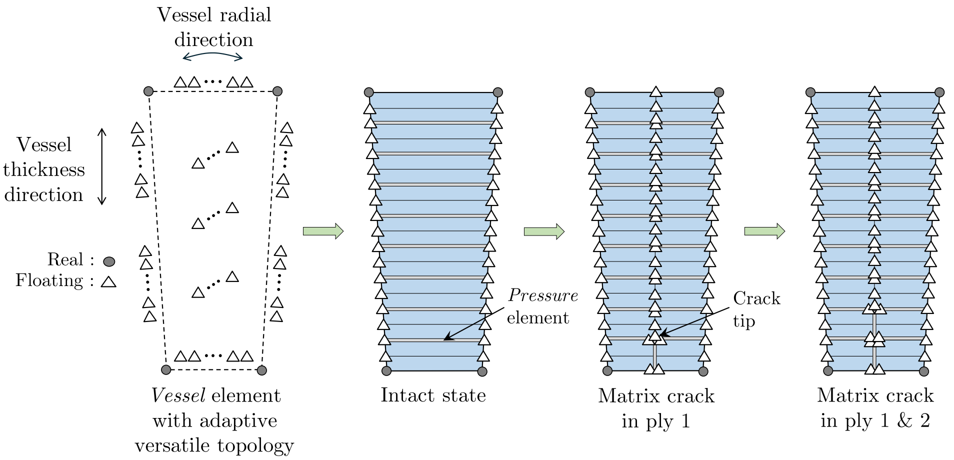

Fig. 17. *Vessel* element topology and its corresponding states for the failure simulation; when the sub-elements fail depending on the thickness location of the crack tip, *vessel* element topology is configured adaptively.

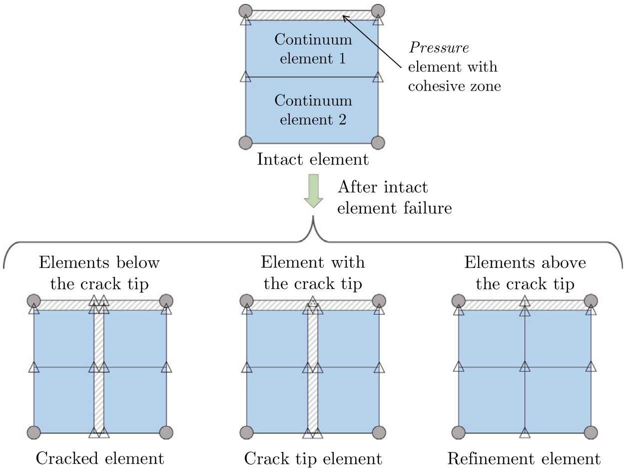

Fig. 18. Various sub-element topologies of the *vessel* element for each ply during the vessel failure simulation; when the continuum sub-elements fail, their topologies are configured adaptively based on the new location of the crack tip.

topologies and partitioning scheme for the failure simulation was provided in Fig. 18. Further illustrations on the *vessel* element implementation, application of *pressure* elements and associated adaptive crack face loading scheme are provided in Figs. 19(a) and 19(b). Here, a 2D application case is used to demonstrate the aforementioned capabilities of the framework; however, the proposed formulation can also be extended to 3D models using the presented approach.

In the numerical model of the *vessel* element, the intact sub-elements (which are exposed to stresses predominantly in the normal circumferential direction σ_h) fracture based on a maximum stress criteria ($\sigma_\mathrm{h} > Y_\mathrm{n}$ or Y_t depending on the ply fibre angle 0° or 90°, respectively). This fracture starts at the first ply as they are exposed to highest stresses and radially propagates towards the outer surface. If any of the integration points experience failure, the *vessel* element automatically inserts a *pressure* element with cohesive zones at the middle of the sub-element domain in that particular ply simulating the emergence of cohesive matrix cracks (see Figs. 17 and 19(a) for state changes). The matrix cracks of the 0° plies experience Mode-I loading, whose critical energy release rate is $91.6\,\mathrm{kJ/m^2}$ [61]. The crack tip essentially lies at the interface between this cracked ply and the ply above (see Fig. 17). Then, the *pressure* elements capturing the matrix cracks and the ply interface above (at the crack tip level) are all pressurized representing the fluid or gas reaching to that point. This pressure acting on the crack faces is essentially the same inner vessel pressure (stored in a global variable during the implementation). The *pressure* elements above the crack tip are not pressurized.

During the numerical analysis, elements that has severe cohesive damage along the interface with the upper plies are removed (Figs. 19(a) and 19(b)). Removal of these ‘loose’ elements from the rest of the model is essential; otherwise, these elements are split and cause numerical convergence problems leading to premature crash of the simulation. Load applied on the bottom face of these elements is not transferred to the upper plies due to the delamination at the element upper interface and artificial high stresses can emerge. Thus, during iterations in an incrementation of the numerical analysis, if the cohesive cracks experience failure subsequently

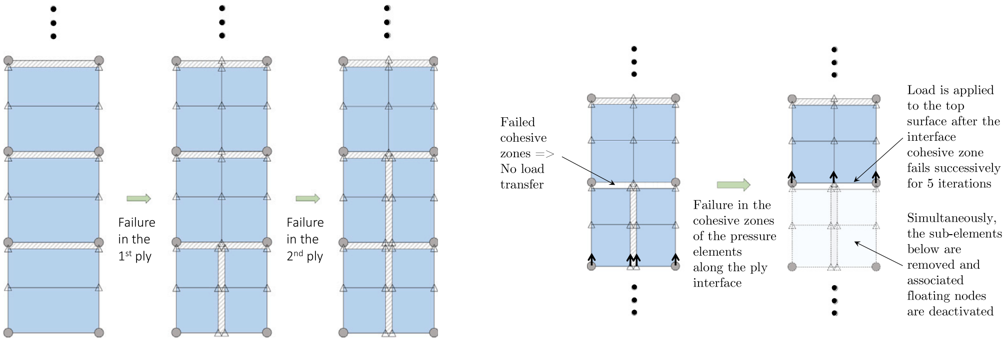

(a) Various sub-element topologies for the vessel failure simulation; based on the crack tip location, sub-elements are configured for different refinement and partitioning schemes adaptively.

(b) Failure and subsequent removal of inner plies during pressure-driven crack propagation.

Fig. 19. Vessel failure simulation using the *vessel* and *pressure* elements.

for 5 iterations, it is removed from the model. In the numerical model, cracks start from inner vessel surface and then, propagate radially to the outer regions. This is accomplished with the introduced partitioning scheme (Fig. 19(a)). The 'loose' element removal is sequentially applied in the radial direction as the cohesive ply interfaces fail from bottom to top plies. Concurrently, crack face loading is also applied to the subsequent ply interfaces and matrix cracks to simulate the pressure-driven propagation of the liquid or gas through the thickness.

9.3. Results and discussion

The deformations of the thin and thick pressure vessels are provided in Figs. 20 and 21. The burst pressure corresponds to the pressure loading at which collective element explosion in the mesh occur due to the extensive cohesive matrix crack and delamination failure. The burst pressure is predicted to be 18.4 MPa and 35.5 MPa for thin and thick vessels, respectively.

The sequential element removal and crack face loading in the radial direction is critical to simulate crack propagation through the thickness without early simulation crash. This procedure is applied as the plies and corresponding interfaces fail through the thickness. However, model can still explode before the last (top-most) plies are removed as the ply interfaces extensively fail throughout the model compromising the structural integrity. Investigations reveal that crack propagation become unstable when the bottom-most 0° ply fails. Then, all laminate and ply interfaces fail in an unstable manner as the model cannot sustain higher pressure loads. The modelling of delamination between the plies as well as their interaction with matrix cracks with cohesive zones are crucial in comprehensive vessel failure assessment; the proposed approach can achieve this thanks to its practical and straightforward framework.

This failure modelling versatility emerges as a distinct capability compared to the other methodologies that does not require re-meshing such as PNM and XFEM. The use of floating nodes based formulation represents exact physical locations of discontinuities that can emerge at different parts of the model on-the-fly without remeshing. Direct physical representation of evolving discontinuities is critical in non-remeshing techniques (XFEM, PNM) for improved accuracy [40]. Complex interaction mechanisms such as matrix crack-delamination interaction can be captured and associated pressure loading (due to liquid or compressed gas) to the exact physical locations of damage surfaces for such complex failure cases can be applied.

The proposed numerical framework also enables modelling of the vessel thickness using only one higher-scale element (*vessel* element). This enables ready information transfer between the sub-elements to model failure. Complex damage scenarios involving matrix and delamination interaction and concurrent application of damage surface loading accounting for this complexity can be achieved through the vessel thickness at element-level in a practical platform. *Vessel* elements with various partitioning and refinement schemes with different sizes can be practically represented using one numerical framework and even modelled in one numerical simulation. Corresponding burst pressure values for each vessel are also determined which can be used as a guideline to design more damage-tolerant vessels. This feature emerges as distinct a capability of the proposed numerical framework when handling pressure-driven fracture compared to the other FEM-based techniques i.e. XFEM and PNM. Valuable insights on vessel failure mechanisms involving high number of cracking and delamination as well as their interaction is attained thanks to this methodology.

10. Conclusions

A new *pressure* element with floating nodes is formulated for modelling pressure-driven fracture and validated with respect to test cases from literature. The key conclusions associated to the developed numerical framework and its capabilities are:

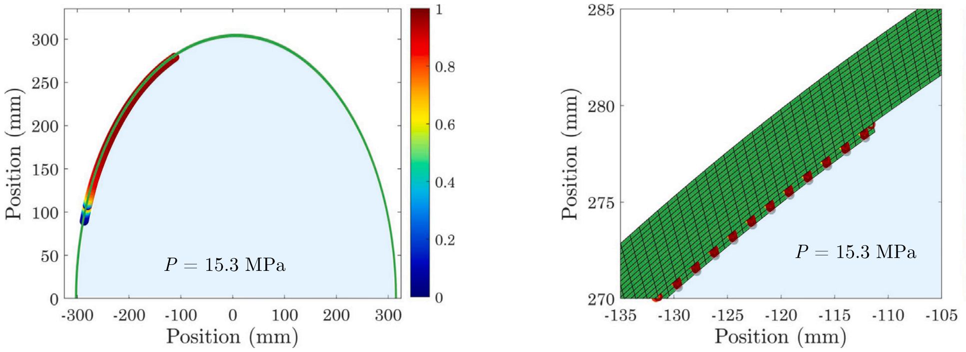

(a) Mesh deformation at 13.3 MPa pressure where cohesive matrix cracking and delamination can be observed in the first layer 90° ply.

(b) Zoomed failure regions in the bottom 90° ply at 13.3 MPa.

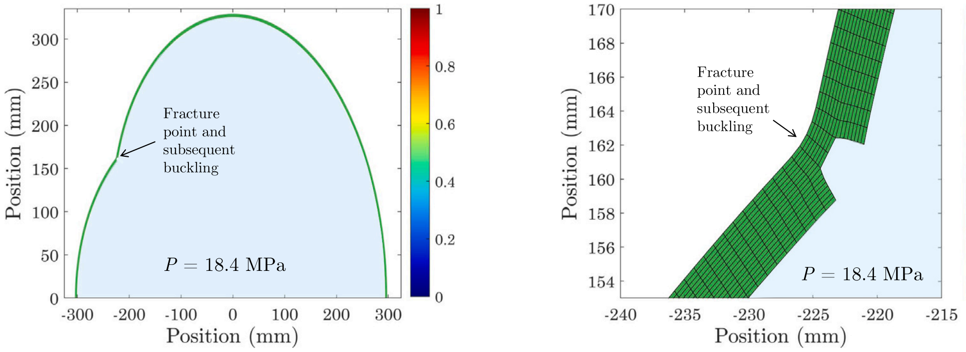

(c) Mesh deformation at 18.4 MPa before burst and significant vessel buckling in the bottom 0° ply can also be observed.

(d) Zoomed failure regions in the bottom 0° ply at 18.4 MPa.

Fig. 20. Deformations and cohesive failure for the thin pressure vessel with 300 mm radius and 0.5 mm ply thickness; damage of the cohesive zones is presented with a colour bar (failed cohesive zones are shown with grey colour).

- the numerical framework provided with the element formulation can integrate *pressure* elements to the physical location of fractures in FE models without remeshing as a user-defined element; it can adaptively apply pressure onto fracture surfaces considering their exact location inside element domains and accurately capture the energy release rates of various slanted cracks exposed to crack face loading;
- the element can also be used in multi-physics problems which is demonstrated in a hydraulic fracture modelling using different numerical solution schemes (iterative and simultaneous); this extended multi-physics framework is verified using a KGD model where associated fracture length, opening width and pressure of hydraulic crack propagation are captured using both solution schemes;
- the numerical framework can inherently enable the application of different solution schemes (iterative and simultaneous); various numerical insights are provided with regards to the implementation of these solution schemes; the results show that higher computational efficiencies can be gained with the simultaneous scheme when multi-physic *pressure* element is used where displacement and pressure DoFs are fully-coupled;
- the proposed numerical framework is also applied in modelling of a key structural problem involving pressure vessel failure; for more effective modelling of vessel systems, a higher-scale *vessel* element is also developed; this element can represent different vessel systems in the thickness direction with the capability to introduce various failure, partitioning and refinement schemes at element level; the sub-elements of this element can easily share information to simulate the damage propagation, introduce required crack face loading and refinement schemes;
- using the numerical framework, methodologies to simulate evolving pressurized cracks and delaminations are presented and burst pressures of different vessels are predicted; investigations reveal the unstable nature of crack propagation particularly after the inner-most 0° ply failure in cohesive modelling of composite vessels;
- this numerical framework can handle evolving complex discontinuities resultant from cohesive cracks and delaminations as well as their interaction in a practical manner; it can adaptively apply pressure to the exact physical locations of newly formed damage surfaces as the pressure-driven fracture propagates; and
- the floating node-based framework can significantly reduce the implementation challenges associated to representing complex evolving discontinuities and their associated crack face loading; it provides a versatile platform which enables more practical

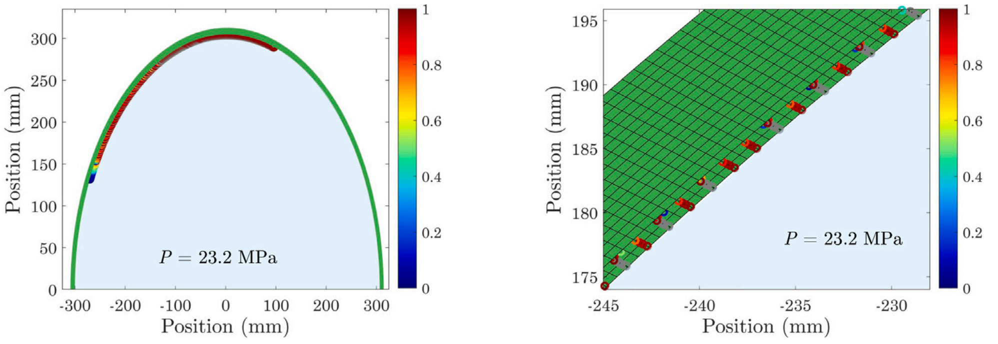

(a) Mesh deformation at 23.2 MPa pressure where cohesive matrix cracking and delamination can be observed in the first layer 90° ply.

(b) Zoomed failure regions in the bottom 90° ply at 23.2 MPa.

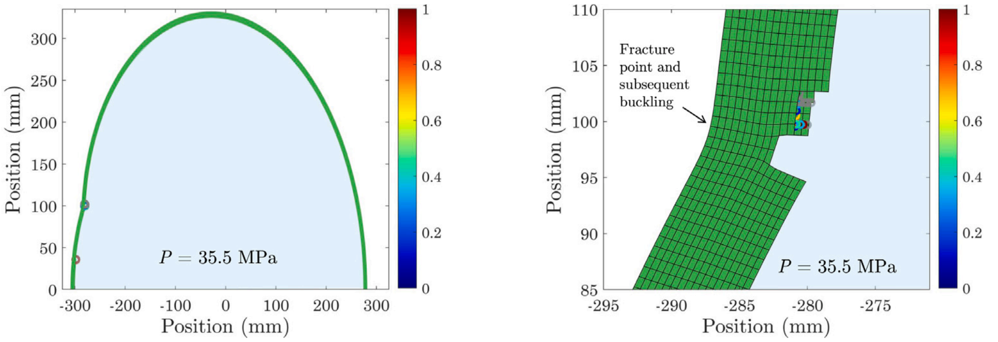

(c) Mesh deformation at 35.5 MPa before burst and significant vessel buckling in the bottom 0° ply can also be observed.

(d) Zoomed failure regions in the bottom 0° ply at 35.5 MPa.

Fig. 21. Deformations and cohesive failure for the thick pressure vessel with 300 mm radius and 1 mm ply thickness; damage of the cohesive zones is presented with a colour bar (failed cohesive zones are shown with grey colour).

and simpler numerical implementation; thanks to this, various element topologies can be engineered such as the higher-scale *vessel* element for more effective modelling of vessel systems.

Overall, this work provides a new practical numerical framework for modelling of pressure-driven failure. Floating node-based approaches can enable simpler platforms to design more-damage tolerant pressurized vessel systems that can be used in sustainable propulsion technologies.

CRediT authorship contribution statement

E.S. Kocaman: Writing – review & editing, Writing – original draft, Visualization, Validation, Supervision, Software, Resources, Project administration, Methodology, Investigation, Funding acquisition, Formal analysis, Data curation, Conceptualization. **B.Y. Chen:** Writing – review & editing, Supervision, Methodology, Investigation, Conceptualization. **S.T. Pinho:** Writing – review & editing, Visualization, Supervision, Project administration, Methodology, Conceptualization.

Declaration of competing interest

The authors declare that they have no known competing financial interests or personal relationships that could have appeared to influence the work reported in this paper.

Acknowledgements

The first author greatly acknowledges funding from Bogazici University under grant BAP_19641SUP. The third author acknowledges funding from EPSRC, United Kingdom project EP/W022508/1.

Data availability

The data that has been used is confidential.

References

[1] P. Liu, J. Chu, S. Hou, P. Xu, J. Zheng, Numerical simulation and optimal design for composite high-pressure hydrogen storage vessel: A review, Renew. Sustain. Energy Rev. 16 (4) (2012) 1817–1827.

[2] V. Cipolla, D. Zanetti, K. Abu Salem, V. Binante, G. Palaia, A parametric approach for conceptual integration and performance studies of liquid hydrogen short–medium range aircraft, Appl. Sci. 12 (14) (2022) 6857.

[3] X. Wang, F. Shi, H. Liu, H. Wu, Numerical simulation of hydraulic fracturing in orthotropic formation based on the extended finite element method, J. Nat. Gas Sci. Eng. 33 (2016) 56–69.

[4] J. Hu, C.G. Mood, M.E. Mear, An efficient computational framework for height-contained growing and intersecting hydraulic fracturing simulation via SGBEM–FEM, Comput. Methods Appl. Mech. Engrg. 419 (2024) 116653.

[5] P. Xu, J. Zheng, P. Liu, Finite element analysis of burst pressure of composite hydrogen storage vessels, Mater. Des. 30 (7) (2009) 2295–2301.

[6] A.A. Krikanov, Composite pressure vessels with higher stiffness, Compos. Struct. 48 (1–3) (2000) 119–127.

[7] Y. Chang, Y. Zhou, N. Wang, K. Lu, W. Wen, Y. Xu, Micro-mechanical damage simulation of filament-wound composite with various winding angle under multi-axial loading, Compos. Struct. 313 (2023) 116925.

[8] A. Onder, O. Sayman, T. Dogan, N. Tarakcioglu, Burst failure load of composite pressure vessels, Compos. Struct. 89 (1) (2009) 159–166.

[9] R. Chang, Experimental and theoretical analyses of first-ply failure of laminated composite pressure vessels, Compos. Struct. 49 (2) (2000) 237–243.

[10] C. Lee, H. Chou, C. Huang, Structural integrity analysis with crack propagation for reactor pressure vessel nozzles based on XFEM, Int. J. Press. Vessels Pip. 207 (2024) 105109.

[11] P. Liu, B. Zhang, J. Zheng, Finite element analysis of plastic collapse and crack behavior of steel pressure vessels and piping using XFEM, J. Fail. Anal. Prev. 12 (2012) 707–718.

[12] D.F. Mora, M. Niffenegger, G. Mao, Simulation of crack propagation in a thick-walled cylinder using XFEM, Procedia Struct. Integr. 42 (2022) 224–235.

[13] F. Daghia, E. Baranger, D.-T. Tran, P. Pichon, A hierarchy of models for the design of composite pressure vessels, Compos. Struct. 235 (2020) 111809.

[14] Z. Chen, et al., An ABAQUS implementation of the XFEM for hydraulic fracture problems, in: ISRM International Conference for Effective and Sustainable Hydraulic Fracturing, International Society for Rock Mechanics, 2013.

[15] T. Mohammadnejad, A. Khoei, An extended finite element method for hydraulic fracture propagation in deformable porous media with the cohesive crack model, Finite Elem. Anal. Des. 73 (2013) 77–95.

[16] D.J. Youn, Hydro-Mechanical Coupled Simulation of Hydraulic Fracturing Using the Extended Finite Element Method (XFEM), Colorado School of Mines, 2016.

[17] A.D. Taleghani, Analysis of Hydraulic Fracture Propagation in Fractured Reservoirs: An Improved Model for the Interaction Between Induced and Natural Fractures, The University of Texas at Austin, 2009.

[18] A. Jafari, M. Vahab, N. Khalili, Fully coupled XFEM formulation for hydraulic fracturing simulation based on a generalized fluid leak-off model, Comput. Methods Appl. Mech. Engrg. 373 (2021) 113447.

[19] M.G. Zielonka, K.H. Searles, J. Ning, S.R. Buechler, Development and validation of fully-coupled hydraulic fracturing simulation capabilities, in: Proceedings of the SIMULIA Community Conference, SCC2014, Providence, Rhode Island, 19-21 May 19-21 2014, 2014.

[20] M. Komijani, R. Gracie, Enriched mixed finite element models for dynamic analysis of continuous and fractured porous media, Comput. Methods Appl. Mech. Engrg. 343 (2019) 74–99.

[21] Z. Chen, A. Bunger, X. Zhang, R. Jeffrey, Cohesive zone finite element-based modeling of hydraulic fractures, Acta Mech. Solida Sin. 22 (5) (2009) 443–452.

[22] B. Carrier, S. Granet, Numerical modeling of hydraulic fracture problem in permeable medium using cohesive zone model, Eng. Fract. Mech. 79 (2012) 312–328.

[23] V.P. Nguyen, H. Lian, T. Rabczuk, S. Bordas, Modelling hydraulic fractures in porous media using flow cohesive interface elements, Eng. Geol. 225 (2017) 68–82.

[24] Q. Zeng, J. Yao, J. Shao, An extended finite element solution for hydraulic fracturing with thermo-hydro-elastic–plastic coupling, Comput. Methods Appl. Mech. Engrg. 364 (2020) 112967.

[25] Y. Heider, A review on phase-field modeling of hydraulic fracturing, Eng. Fract. Mech. 253 (2021) 107881.

[26] Z.A. Wilson, C.M. Landis, Phase-field modeling of hydraulic fracture, J. Mech. Phys. Solids 96 (2016) 264–290.

[27] L.-P. Yi, H. Waisman, Z.-Z. Yang, X.-G. Li, A consistent phase field model for hydraulic fracture propagation in poroelastic media, Comput. Methods Appl. Mech. Engrg. 372 (2020) 113396.

[28] C. Chukwudozie, B. Bourdin, K. Yoshioka, A variational phase-field model for hydraulic fracturing in porous media, Comput. Methods Appl. Mech. Engrg. 347 (2019) 957–982.

[29] M. Qin, D. Yang, W. Chen, X. Xia, Hydraulic fracturing network modeling based on peridynamics, Eng. Fract. Mech. 247 (2021) 107676.

[30] M. Qin, D. Yang, W. Chen, Three-dimensional hydraulic fracturing modeling based on peridynamics, Eng. Anal. Bound. Elem. 141 (2022) 153–166.

[31] H. Ouchi, A. Katiyar, J.T. Foster, M.M. Sharma, A peridynamics model for the propagation of hydraulic fractures in heterogeneous, naturally fractured reservoirs, in: SPE Hydraulic Fracturing Technology Conference and Exhibition, SPE, 2015, D011S001R006.

[32] S. Cheng, M. Zhang, X. Zhang, B. Wu, Z. Chen, Z. Lei, P. Tan, Numerical study of hydraulic fracturing near a wellbore using dual boundary element method, Int. J. Solids Struct. 239 (2022) 111479.

[33] B. Lecampion, A. Bunger, X. Zhang, Numerical methods for hydraulic fracture propagation: A review of recent trends, J. Nat. Gas Sci. Eng. 49 (2018) 66–83.

[34] C. Dong, C. De Pater, Numerical implementation of displacement discontinuity method and its application in hydraulic fracturing, Comput. Methods Appl. Mech. Engrg. 191 (8–10) (2001) 745–760.

[35] L. Xie, K.-B. Min, B. Shen, Simulation of hydraulic fracturing and its interactions with a pre-existing fracture using displacement discontinuity method, J. Nat. Gas Sci. Eng. 36 (2016) 1284–1294.

[36] A. Abdollahipour, M.F. Marji, A.Y. Bafghi, J. Gholamnejad, Simulating the propagation of hydraulic fractures from a circular wellbore using the displacement discontinuity method, Int. J. Rock Mech. Min. Sci. 80 (2015) 281–291.

[37] K. Wu, J.E. Olson, A simplified three-dimensional displacement discontinuity method for multiple fracture simulations, Int. J. Fract. 193 (2015) 191–204.

[38] J.M. Segura, I. Carol, Coupled HM analysis using zero-thickness interface elements with double nodes. Part I: Theoretical model, Int. J. Numer. Anal. Methods Geomech. 32 (18) (2008) 2083–2101.

[39] J. Segura, I. Carol, Coupled HM analysis using zero-thickness interface elements with double nodes—Part II: Verification and application, Int. J. Numer. Anal. Methods Geomech. 32 (18) (2008) 2103–2123.

[40] B. Chen, S. Pinho, N. De Carvalho, P. Baiz, T. Tay, A floating node method for the modelling of discontinuities in composites, Eng. Fract. Mech. 127 (2014) 104–134.

[41] R. da Costa, S. Pinho, A novel formulation for the explicit discretisation of evolving boundaries with application to topology optimisation, Comput. Methods Appl. Mech. Engrg. 367 (2020) 113077.

[42] N. De Carvalho, B. Chen, S. Pinho, J. Ratcliffe, P. Baiz, T. Tay, Modeling delamination migration in cross-ply tape laminates, Composites A 71 (2015) 192–203.

[43] B. Chen, T. Tay, S. Pinho, V. Tan, Modelling the tensile failure of composites with the floating node method, Comput. Methods Appl. Mech. Engrg. 308 (2016) 414–442.

[44] M. McElroy, An Enriched Shell Finite Element for Progressive Damage Simulation in Composite Laminates, NASA/TP-2016-219211, Langley Research Center, 2016.

[45] B. Chen, T. Tay, S. Pinho, V. Tan, Modelling delamination migration in angle-ply laminates, Compos. Sci. Technol. 142 (2017) 145–155.

[46] X. Lu, B. Chen, V. Tan, T. Tay, Adaptive floating node method for modelling cohesive fracture of composite materials, Eng. Fract. Mech. 194 (2018) 240–261.

[47] X. Lu, B. Chen, V. Tan, T. Tay, A separable cohesive element for modelling coupled failure in laminated composite materials, Composites A 107 (2018) 387–398.

[48] R. da Costa, S. Pinho, Topology optimisation for robust design of large composite structures, Compos. Struct. 321 (2023) 117314.

[49] M. Ortiz, A. Pandolfi, Caltech ASCI technical report 090, Internat. J. Numer. Methods Engrg. 44 (1999).

[50] R. Krueger, Virtual crack closure technique: history, approach, and applications, Appl. Mech. Rev. 57 (2) (2004) 109–143.

[51] K. Park, G.H. Paulino, Computational implementation of the PPR potential-based cohesive model in ABAQUS: Educational perspective, Eng. Fract. Mech. 93 (2012) 239–262.

[52] C.K. Batchelor, G. Batchelor, An Introduction to Fluid Dynamics, Cambridge University Press, 2000.

[53] I. Raju, Calculation of strain-energy release rates with higher order and singular finite elements, Eng. Fract. Mech. 28 (3) (1987) 251–274.

[54] J. Geertsma, F. De Klerk, et al., A rapid method of predicting width and extent of hydraulically induced fractures, J. Pet. Technol. 21 (12) (1969) 1–571.

[55] E. Detournay, Propagation regimes of fluid-driven fractures in impermeable rocks, Int. J. Geomech. 4 (1) (2004) 35–45.

[56] T.L. Anderson, T.L. Anderson, Fracture Mechanics: Fundamentals and Applications, CRC Press, 2005.

[57] E.E. Gdoutos, Fracture Mechanics: An Introduction, vol. 123, Springer Science & Business Media, 2006.

[58] E. Alizadeh, M. Dehestani, Analytical and numerical fracture analysis of pressure vessel containing wall crack and reinforcement with CFRP laminates, Thin-Walled Struct. 127 (2018) 210–220.

[59] R. Krueger, Development and Application of Benchmark Examples for Mixed-Mode I/II Quasi-Static Delamination Propagation Predictions, NASA/CR-2012-217562, NASA, 2012, 2012.

[60] Hexcel, HexPly® 8552, Hexcel Corporation Product Data Sheet, 2023.

[61] S.T. Pinho, P. Robinson, L. Iannucci, Fracture toughness of the tensile and compressive fibre failure modes in laminated composites, Compos. Sci. Technol. 66 (13) (2006) 2069–2079.